



# Experimentally Closing the Balance of Progress of Reaction in Premixed Turbulent Combustion in the Thin Flame Regime

Yutao Zheng<sup>1</sup> · Lee Weller<sup>1</sup> · Simone Hochgreb<sup>1</sup>

Received: 17 August 2023 / Accepted: 21 February 2024 / Published online: 25 March 2024  
© The Author(s) 2024, corrected publication 2024

## Abstract

We investigate the possibility of determining the local turbulent flame speed by measuring the individual terms in the balance of a mean progress of reaction variable for the case of a low turbulence methane-air Bunsen flame in the thin flame regime. Velocity distributions and flame edge positions were measured by particle image velocimetry techniques at 3 kHz for a flame stabilized by a surrounding pilot of the same stoichiometry, for a turbulent Reynolds number around 66 and Karlovitz numbers of the order of 4. The conservation equation for mean progress variable was analyzed along different streamlines as a balance of terms expressed as velocities, including terms for convection, turbulent diffusion, mean reaction, and turbulent and molecular diffusion. Each term was estimated from local velocities and flame locations using a thin flame approximation, and their uncertainty was evaluated based on propagation of experimentally measured statistical correlations. The largest terms were the convective and reaction terms, as expected, with smaller roles for turbulent and molecular diffusion across the flame brush. Countergradient diffusion and transition to gradient diffusion were observed across the flame brush. Closure of the balance of terms in the conservation equations using independently measured terms was not consistently achieved across the flame brush within the reckoned uncertainties, arriving at a balance within 20–30% of the absolute value. Testable hypotheses are offered for the possible reasons for the mismatch, including the role of spatial filtering and 3D effects on the reaction rate term. Finally, the experiments identify the inaccuracies in measuring a true local turbulent flame speed, and suggest a consistent methodology to reduce errors in such estimations. This is the first time such a detailed experimental closure is attempted for any configuration. The results suggest that the significant improvements in spatial resolution are necessary for a full closure.

**Keywords** Turbulent premixed flames · Turbulent flame speed · High speed PIV · Turbulent reaction progress variable

## 1 Introduction

The accurate experimental determination of the local turbulent flame speeds under arbitrary turbulence and flow conditions remains a difficult challenge. The turbulent Bunsen flame is one of the well-investigated configurations for understanding the behaviour of premixed turbulent flames. The geometry provides an enveloped, statistically stationary flame in which burning velocities can in principle be well-defined by the velocities at the leading edge of the flame brush. The fact that all reactants are surrounded by the flame means that one can relate the total mass flow of reactants to the reacting surface, and the statistically stationary character of the flame enables the application of optical diagnostic methods to characterize the flame properties.

The flow and turbulent characteristics of turbulent premixed Bunsen flames have been widely investigated in experimental work (Kobayashi et al. 1996, 2005; Filatyev et al. 2005; Yuen 2009; Troiani et al. 2013; Wabel 2017), as well as in Direct Numerical Simulations (DNS) (Sankaran et al. 2007; Veynante et al. 2010; Klein et al. 2018a, b; Chakraborty et al. 2019). However, most experimental investigations have focused on simply measuring global turbulent burning velocities, by dividing the total mass flow rate by a selected surface area.

Nevertheless, there can be large differences in the local burning rate around the surface of the flame brush, and the one global measurement can differ significantly from the local values. A clear definition of turbulent burning velocities should be made by analysing the behavior of the flame brush around the full envelope. Previous work by Shepherd and coworkers used laser Doppler anemometry combined with OH planar laser induced fluorescence (OH PLIF) to estimate local values of different terms in the balance of mean progress variables in premixed flames, using various geometries (Shepherd et al. 1992; Shepherd 1996; Shepherd et al. 1998; Cheng and Shepherd 1991). Here we revisit that idea using high-frequency Mie scatter and particle image velocimetry (PIV) as a single diagnostic to measure both flow velocities and flame location.

Experimental measurements of different terms in the mean progress of reaction  $\bar{c}$ -balance equation have been conducted previously (Gouldin 1996; Veynante et al. 1996; Most et al. 2002), both regarding the turbulent flux term (Louch and Bray 1998; Kalt and Bilger 2000), as well as in combination (Shepherd et al. 1992; Shepherd 1996; Shepherd et al. 1998; Cheng and Shepherd 1991). In all of these studies, either Mie scatter or OH PLIF has been used to determine the location of the interface of the flame, which is treated as infinitely thin interface, with a bimodal distribution of progress of reaction variable represented by product and reactant. The approximation has been experimentally shown to be sound for sufficiently low  $Ka$ , as demonstrated for example by Sweeney et al. (2013) and Skiba et al. (2021). Based on the aforementioned experimental evidence, and in common with all of the previous experiments and analyses cited in the present paragraph, the current work therefore assumes that a bimodal distribution is sufficiently accurate to represent the statistics of mean progress of reaction.

Gouldin and coworkers (Miles 1991; Gouldin 1996) measured conditional velocities in turbulent statistically stationary V-flames and evaluated the total reaction rate and the turbulent flux term. The study pointed out the feasibility of measuring burning rates indirectly from the sum of convection terms and turbulent flux terms.

Veynante et al. (1996) measured turbulent fluxes in a V-flame. Flame edges were detected by Mie scattering of small oil droplets, and unburnt gas velocities were measured by laser Doppler velocimetry. The gradient and counter gradient diffusion

effect of the scalar transport was observed in different locations of the V-flame. The study pointed out that the gradient diffusion existed near the rod where the geometrical effect was stronger, and the countergradient diffusion existed where thermal expansion dominated the flow.

Kalt and coworkers (Kalt et al. 1998; Kalt and Bilger 2000) quantified the countergradient diffusion parameters and the Bray number to provide a detailed illustration of the transition of countergradient diffusion to gradient diffusion and the feasibility of modelling the turbulent flux term as a function of progress of reaction, laminar flame speed and turbulence intensity.

Most et al. (2002) applied simultaneous planar filtered Rayleigh scattering thermometry (FRS) and particle image velocimetry (PIV) to measure flame edges and velocity distributions simultaneously, and determined the turbulent flux for a wire-stabilized V-shaped flame at moderate turbulence, as well as a highly turbulent bluff-body-stabilized flame. The turbulent flux was directly determined from the product of Favre-averaged temperature and mean velocity-progress variable correlation, and was also evaluated from the flamelet assumption. Turbulent fluxes extracted from direct temperature and velocity measurements were compared to values using the flamelet assumption, showing reasonable agreement and confirming the feasibility of evaluating turbulent flux terms based on these two different approaches.

A number of DNS simulations have also been used to investigate different terms of the conservation equation of the mean progress of reaction  $\bar{c}$  (Dunstan et al. 2011; Mukhopadhyay et al. 2015; Chakraborty et al. 2019; Rasool et al. 2022). Dunstan et al. (2011) converted the conservation of the Favre-averaged mean progress variable  $\bar{c}$  into velocity terms, and evaluated the balance of different terms using DNS results for a V-flame for turbulent Reynolds numbers within 18~92. DNS results showed that, whereas in general the leading order terms are the convection and reaction terms, the turbulent flux plays an important role at the leading edge of the flame brush as the turbulent intensity increased. A turbulent consumption speed,  $s_c$ , calculated from the integral of the mean reaction rate across the flame brush, was compared with  $s_T$ , showing a large quantitative difference. Such comparisons were also conducted on other stationary flames (Dunstan et al. 2012), but rarely for Bunsen flames (Sankaran et al. 2007).

In the present study, we measure velocity distributions and instantaneous flame edge locations on a plane simultaneously in a premixed turbulent Bunsen flame by using high-frequency planar particle image velocimetry (PIV). Flame edges are detected by a number density method based on the number densities of solid particles. Using velocity and flame location, the different terms on both sides of the conservation equation for the progress of reaction are reckoned inside the flame brush ( $0.1 < \bar{c} < 0.9$ ), including turbulent flux (scalar transport), molecular diffusion, and mean reaction rates. In particular, these terms are evaluated along streamlines selected for higher accuracy of measurement, and extrapolated using well-established models to the leading and trailing edge of the flame brush. In that process, we establish which terms are of leading order along the flame brush.

It is found that exact closure cannot be easily realized across the flame brush, and specific sources of discrepancies are discussed. An uncertainty analysis is conducted in detail to illustrate the accuracy of the extrapolation from the measured region to the leading and trailing edge of the flame brush. The results show that it is possible to unambiguously associate a leading edge velocity to each streamline, but that the value cannot be easily related to the estimates of consumption velocity.

## 2 Balance of Mean Progress of Reaction

A progress variable can be defined in a number of different ways. In the present development, a thin flame assumption and bimodal distribution of the progress of reaction variable is made throughout the study (often called the BML assumption, after the Bray–Moss–Libby model (Bray and Moss 1977; Bray et al. 1984), which is consistent with moderate turbulent conditions. Under these conditions, any well-defined and properly scaled variable (temperature, density) representative of the burnt or unburnt gas can be used as a marker of progress of reaction. The relevant conservation for the progress of reaction becomes (Poinso and Veynante 2005):

$$\frac{\partial \rho c}{\partial t} + \nabla \cdot (\rho \mathbf{u} c) = \nabla \cdot (\rho D_c \nabla c) + \dot{\omega}_c \quad (1)$$

where density is  $\rho$ , velocity  $\mathbf{u}$ , diffusivity of  $c$  is  $D_c$  (differential diffusion effects are neglected), and the final term  $\dot{\omega}_c$  is the reaction rate per unit volume. A density-weighted variable  $\tilde{c}$  is defined as:

$$\tilde{c} = \frac{1}{\bar{\rho}} \int_0^1 \rho c p(c) dc \quad (2)$$

where  $p(c)$  is the probability density function of  $c$  and  $\bar{\rho}$  the local mean density.

The corresponding equation for the conservation equation under turbulent conditions represented by a mean and a fluctuating term is obtained by taking the density-weighted (Favre) ensemble average of Eq. (1),

$$\frac{\partial \bar{\rho} \tilde{c}}{\partial t} + \nabla \cdot (\bar{\rho} \tilde{\mathbf{u}} \tilde{c}) = -\nabla \cdot (\bar{\rho} \tilde{\mathbf{u}}'' c'') + \nabla \cdot (\bar{\rho} D_c \nabla c) + \bar{\omega}_c \quad (3)$$

where  $\mathbf{T}_c^F = \bar{\rho} \tilde{\mathbf{u}}'' c''$  corresponds to the mean turbulent flux,  $\mathbf{T}_c^D = \bar{\rho} D_c \nabla c$  to mean molecular diffusion, and  $\bar{\omega}_c$  is the mean reaction rate.

Equation (3) can be reformulated by subtracting the mean conservation of mass to obtain:

$$\bar{\rho} \left( \frac{\partial \tilde{c}}{\partial t} + \tilde{\mathbf{u}} \cdot \nabla \tilde{c} \right) = -\nabla \cdot \mathbf{T}_c^F + \nabla \cdot \mathbf{T}_c^D + \bar{\omega}_c \quad (4)$$

$$s_T \equiv \frac{1}{|\nabla \tilde{c}|} \frac{\tilde{D} \tilde{c}}{Dt} = s_F + s_D + s_R \quad (5)$$

After dividing by  $\bar{\rho} |\nabla \tilde{c}|$ , the terms are converted into velocities. The left hand side term  $s_T$  is defined as the convective turbulent displacement speed, and  $s_F$ ,  $s_D$  and  $s_R$  are terms of turbulent burning velocity corresponding to turbulent fluxes, molecular diffusion and reaction, respectively. The operator  $\tilde{D}/Dt = \partial/\partial t + \tilde{\mathbf{u}} \cdot \nabla(\cdot)$  is defined to avoid confusion with the substantial derivative operator (Anderson and Wendt 1995; Lipatnikov and Chomiak 2010),  $D/Dt(\cdot) = (\partial/\partial t + \mathbf{u} \cdot \nabla)(\cdot)$ .

For a statistically stationary flame, such as strained flat flames and Bunsen flames, unsteady term  $\partial/\partial t$  can be neglected. We obtain four terms in Eq. (5) as

$$s_T = \tilde{\mathbf{u}} \cdot \frac{\nabla \tilde{c}}{|\nabla \tilde{c}|} = \tilde{\mathbf{u}} \cdot \hat{\mathbf{n}} \quad (6a)$$

$$s_R = \frac{\bar{\dot{\omega}}_c}{\bar{\rho}|\nabla\tilde{c}|} \quad (6b)$$

$$s_F = \frac{-\nabla \cdot T_c^F}{\bar{\rho}|\nabla\tilde{c}|} \quad (6c)$$

$$s_D = \frac{\nabla \cdot T_c^D}{\bar{\rho}|\nabla\tilde{c}|} \quad (6d)$$

The normal vector  $\hat{\mathbf{n}}$  of the  $\tilde{c}$ -isosurface towards the product is defined as  $\nabla\tilde{c}/|\nabla\tilde{c}|$ , pointing towards the product side for convenience with the particular geometric orientation of the flow.

For situations in which the flamelet assumption is valid, the turbulent flux can be related to the bimodal conditioned mean properties of the burnt and unburnt mixture, as also applied in previous work (Gouldin 1996; Veynante et al. 1996; Most et al. 2002).

$$\overline{\rho \mathbf{u}'' c''} = \bar{\rho} \tilde{c} (1 - \tilde{c})(\bar{\mathbf{u}}_b - \bar{\mathbf{u}}_u) \quad (7)$$

Finally, one can invoke a flame surface density model for the reaction rate term based on the BML model,  $\bar{\dot{\omega}}_c = \rho_u s_L I_0 \Sigma$  into Eq. (6b), to obtain a measurable form of  $s_R$ ,

$$s_R = s_L \frac{\rho_u}{\bar{\rho}} \frac{\Sigma}{|\nabla\tilde{c}|} \quad (8)$$

where  $s_L$  is the unstrained laminar flame speed,  $\Sigma$  the flame surface density and  $I_0$  a correction factor. In the present work, we are not interested in determining  $I_0$ , but instead, for this low turbulence case, to estimate how well the balance of terms is able to capture the overall behavior without modeling  $I_0$ , which taken as unity.

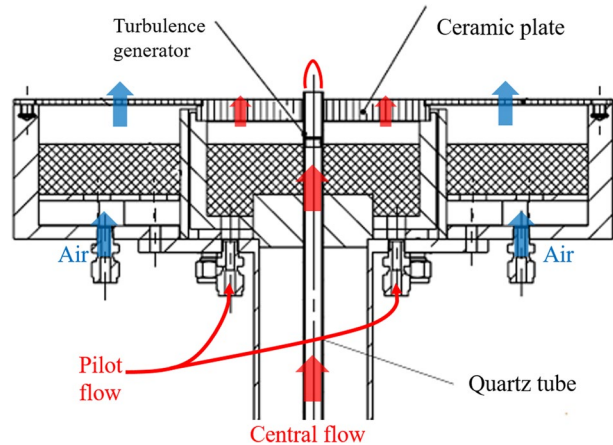
In what follows, we use 2D Mie scatter of particles to investigate a statistically stationary, cylindrically symmetrical Bunsen flame to provide instantaneous measurements of velocity and flame edge locations. We use these measurements to calculate terms in Eq. (3), and investigate to what extent one can test the local balance of terms along streamlines.

## 3 Experimental Methodology

### 3.1 Burner Setup

The burner setup is shown in Fig. 1. The central methane/air flame consists of a turbulent methane/air Bunsen flame generated by a quartz tube of 10 mm internal diameter (Zheng et al. 2022). A pilot methane/air flame at the same equivalence ratio as the central flame surrounds the central tube, stabilised by a porous ceramic plate. The central flame and the pilot flame were enclosed by a low velocity air flow stream.

**Fig. 1** Cutaway of the symmetry plane of the burner setup showing central quartz tube, pilot flame support and outer co-flow. Inset shows cross section of the perforated plate, with dimensions in mm



### 3.2 PIV Measurements

PIV measurements were conducted to determine planar velocity distributions on the vertical plane ( $r-z$  plane) by calculating the cross-correlation between two Mie scatter images acquired from a high-speed double frame camera.

A Litron LDY 300 dual-head laser operated at 3 kHz was used to produce 527 nm wavelength, 300 ns-long pulses. The beam exiting the laser head ( $d \approx 4$  mm) was expanded by a plano-concave cylindrical lens ( $f_1 = -25$  mm) and reshaped by a plano-convex cylindrical lens ( $f_2 = 50.8$  mm) into a 50 mm height  $\times$  4 mm thickness laser sheet. Finally, the laser sheet was focused by a plano-convex cylindrical lens ( $f_3 = 500$  mm) into the desired top-hat beam intensity of 40 mm height  $\times$  0.5 mm thickness at the flame location, after clipping at the edges. A high speed Phantom V611 camera (LaVision) was used to record Mie scatter images using a visible lens objective with focal lens distance of 60 mm, which was doubled to 120 mm by adding a  $2\times$  tele-converter, using a maximum aperture of  $f/2.8$  mm.

The imaged region is  $1280 \times 800$  pixel<sup>2</sup> and covered 50 mm  $\times$  32 mm (H  $\times$  L), with a spatial resolution of 39  $\mu\text{m}$ /pixel across the symmetry plane. The Mie scatter image for each particle occupied around 2 to 3 pixels squared. Five non-reacting background images were collected and averaged for subtraction before recording Mie scatter images. The background noise is negligible compared to the fluctuation of the signal.

The PIV cross-correlation was conducted using the LaVision Davis 8.3 software. The interrogation window size for PIV cross-correlation was chosen as  $16 \times 16$  pixels ( $0.62 \times 0.62$  mm) with 50% overlap. The seeding system delivered 14 to 16 particles per interrogation window in the reactant side or about 16 pixels<sup>2</sup> per particle. The upper limit of peak ratio of Q-values was set at its default value of 1.2. The chosen particle density was shown to be a good compromise between providing sufficiently spaced particles for PIV interrogation whilst sufficiently dense to determine the flame edge.

### 3.3 Flame Edge Detection and Flame Surface Density Measurement

Flame edges were detected based on the first frame of the Mie scattering images. Each instantaneous flame edge was determined based on the number density of solid particles

by using the number density method (Pfadler et al. 2007; Steinberg et al. 2008), which detects the interface of high gradient in number density associated with temperature change at the flame surface (Pfadler et al. 2007; Steinberg et al. 2008).

In this study, the parameters used for the number density method were tuned for edge detection by comparison with simultaneous OH-PLIF measurements in previous experiments (Zheng et al. 2022). A square window of  $w_d = 40$  pixels (1.56 mm) was chosen as the minimum width for obtaining a sufficient number of particles. Flame edges were determined at the point of maximum gradient of number density, corresponding to the maximum fluid density change. A previous assessment of the distribution of minimum 2D distances between flame edges detected by the number density method and OH-PLIF (Zheng et al. 2022) showed that the number method produced edge locations within a distance of half of the laminar flame thickness (about 0.25 mm), with only around 10% of images producing distance discrepancies larger than the laminar flame thickness. The same study also showed that local flame surface density and flame curvature distributions obtained between the two methods agreed within a few percent of the local mean value.

Based on these studies, we estimate that by using the number density method, flame edges were detected near the maximum heat release point within half of the laminar thickness, corresponding to a Gaussian filter with a width of 0.22–0.27 mm.

Each 2D image is expressed in matrix form and binarized into reactant and product side based on the detected flame edge, consisting of a pixel of finite dimensions, yielding a matrix  $c(\mathbf{x}) = \mathbf{B}$  where  $\mathbf{B}$  is a matrix of Boolean variables.

The mean (ensemble-averaged) progress variable is calculated at each position  $\mathbf{x}$  according to Eq. (9) for  $N$  images.

$$\bar{c} = \int_0^1 cp(c) dc \approx \frac{1}{N} \sum_{i=1}^N \mathbf{B}_i \quad (9)$$

where  $p(c)$  is the probability of finding the reactant or product.

The mean Favre-averaged local progress variable is calculated accordingly from Eq. (2) as:

$$\bar{c} = \int_0^1 \frac{\rho}{\bar{\rho}} cp(c) dc = \frac{1}{N} \sum_{i=1}^N \left[ \frac{\mathbf{B}_i}{\Theta} \left( 1 + \mathbf{B}_i \left( \frac{1}{\Theta} - 1 \right) \right)^{-1} \right] \quad (10)$$

where  $\Theta = \rho_u/\rho_b$  is the density ratio between unburnt and burnt gas, here taken to be the ratio of equilibrium densities at the relevant equivalence ratio.

The mean local flame surface density (FSD),  $\Sigma$ , was determined as the averaged 2D gradient of progress variable  $c$ .

$$\Sigma_{2D} = \overline{\Sigma'_{2D}} = \overline{|\nabla c \delta(c - c^*)|} \approx \frac{1}{N} \sum_{i=1}^N |\nabla \mathbf{B}_i| \quad (11)$$

where  $\mathbf{B}$  is the binarized matrix described in Eq. (9), and the operator gradient of a discrete variable in 2D is described in *Supplementary Material*.

We also observe that, given the spatial limitation of the number density method, flame edges near the anchoring point of the flame, where the contribution to the total flame area can be estimated as laminar flame, can not be accurately determined, so edge detection was only performed at distances beyond 3 mm from the flame stabilization point.

### 3.4 Experimental Conditions

Table 1 lists experimental conditions considered. A total of 4000 images were collected to ensure convergence of the first and second moments of velocity and progress of reaction. The streamwise integral time and length scales  $\tau_0 \approx 0.3$  ms and  $l_0 \approx 1.3$  mm were measured along the central line of the burner based on the definition of the time (and respectively space) autocorrelation of the axial velocity using a sequence of 1000 images (until the distribution of  $\bar{c}$  is converged). The turbulent Reynolds number  $Re_T$  for the flow is defined as  $Re_T = \frac{u' l_0}{\nu}$ , where  $u'$  is the measured free stream turbulence level,  $l_0 = 1.3$  mm is the measured integral length scale and  $\nu$  is the kinematic viscosity of the free stream reactant mixture.

The mean turbulent intensity  $u'$  is calculated from the 2D velocity measurements as

$$u' = \sqrt{v_{r,rms}^2 + v_{z,rms}^2} \quad (12)$$

The Karlovitz number,  $Ka = \tau_f / \tau_\eta$  (Peters 2000), is calculated as the ratio of the flame time scale,  $\tau_f$ , to the Kolmogorov or viscous time scale,  $\tau_\eta$ , which is estimated as  $\tau_\eta = \tau_0 Re_T^{-1/2}$  where  $\tau_0 = 0.3$  ms is the integral time scale. The flame time scale is estimated as  $\tau_f = \alpha / s_L^2$ , where  $\alpha$  is the thermal diffusivity in the fresh reactants, and  $s_L$  is the corresponding laminar flame speed. The thermal diffusivity is estimated as  $\alpha = \nu / Pr$ , where  $Pr$  is the Prandtl Number taken as equal to 0.71 for the reactant mixtures considered in the present study and the viscosity  $\nu$  was taken at an ambient temperature of  $T_a = 15$  °C. The mixed viscosity of fuel/air mixture was derived used the Gambill Method (Gambill 1959), and found to be  $(15.64 \pm 0.01) \times 10^{-6}$  m<sup>2</sup>/s for all cases.

### 3.5 Uncertainty Analysis

Uncertainties in local instantaneous velocities depend on the time interval used for PIV and the interrogation volume. In the present work,  $\Delta t = 33$   $\mu$ s, and mean axial velocities of the order of 5 m/s, corresponding to mean displacement distances  $L_m = 0.15$  mm in the interrogation area, which corresponds to 4~5 pixels (1/4 of interrogation window). Since each particle normally occupies 2 to 3 pixels in the interrogation area when conducting PIV cross-correlation, the uncertainty of the average moving distance between two pulses is of the order of less than 1 pixel (Raffel et al. 2018). In this study, we assume the uncertainty of mean displacement in each interrogation window is in order of 0.5 pixels, which is the maximum uncertainty in 16×16 pixel interrogation window (Wieneke 2015). Therefore,

**Table 1** Experimental cases

	$\Phi$	$\bar{U}_0$	$v_{z,rms}$	$u'$	$s_L^{(1)}$	$l_0$	$\delta_L^{(1)}$	$\Theta$	$Re_T$	$Ka$
	(–)	(m/s)	(m/s)	(m/s)	(m/s)	(mm)	(mm)			
Case 1	0.9	5.3	0.52	0.81	0.320	1.3	0.479	7.27	67.5	4.2
Case 2	1.2	5.5	0.49	0.78	0.319	1.3	0.477	7.39	65.0	4.1

<sup>(1)</sup>  $s_L$  and  $\delta_L = (T_b - T_u) / |\nabla T|_{\max}$  were calculated using Cantera 2.5.1 (Goodwin et al. 2021) and GRI Mech 3.0 (Smith et al. 1999)



the estimated intrinsic error in local velocities in the order of  $0.5\Delta x/\Delta t \approx 0.58$  m/s, which is relatively small compared with local mean velocities.

Conditional averaging was conducted for variables along a local streamline using local discretized approximations of a direct measurable factor  $\varphi_i$ . For an indirectly measured factors  $q = f(\varphi_i)$  where  $f$  is a nonlinear function of variables  $\varphi_i$ , such as local mass flow rates and velocity normal to an isosurface, the total uncertainty was derived from error propagation based on uncertainties of directly measurable variables (Ku et al. 1966):

$$\sigma_q = \sqrt{\sum_{i=1}^{N_\varphi} \left(\frac{\partial f}{\partial \varphi_i}\right)^2 \sigma_{\varphi_i}^2 + 2 \sum_{i=1}^{N_\varphi} \sum_{j=i}^{N_\varphi} \sigma_{\varphi_i\varphi_j}^2 \left(\frac{\partial f}{\partial \varphi_i}\right) \left(\frac{\partial f}{\partial \varphi_j}\right)} \tag{13}$$

where  $\sigma_{\varphi_i\varphi_j}$  is covariance between  $\varphi_i$  and  $\varphi_j$  and will be considered in this study when  $\varphi_i$  and  $\varphi_j$  are actually correlated.  $\sigma_{\varphi_i\varphi_j}$  is derived from *Matlab* function *cov*( $\varphi_i, \varphi_j$ ).

When evaluating the uncertainty of an integral, the auto correlation of the uncertainty of  $\varphi$  is considered to be the maximum based on the Cauchy-Schwarz inequality, and we assume limit of the inequality in Eq. (14), and the uncertainty of the integral  $\sigma_q$  is estimated as the square root of the integral of the square of uncertainties of  $\varphi$ .

$$q = \int_0^1 \varphi(x) dx \Rightarrow \sigma_q \leq \sqrt{\int_0^1 \sigma_\varphi^2(x) dx} \tag{14}$$

## 4 Results

### 4.1 Flame Brush Characterisation

Figure 2 shows the 2D distribution of mean progress of reaction over the domain at each coordinate point  $\mathbf{x} = (r, z)$  across the flame brush for Case 1. Figure 2 exhibits a discernible degree of asymmetry, which could plausibly be attributed to the challenge of aligning

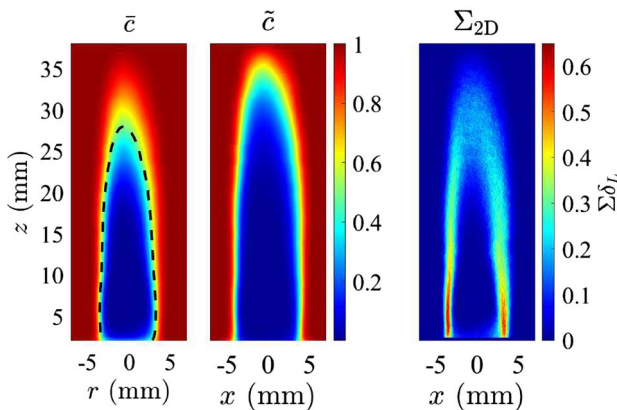


**Fig. 2** Mean ( $\bar{c}$ ) and Favre-averaged ( $\tilde{c}$ ) progress variable, and flame surface density  $\Sigma_{2D}$  for Case 1. Black dashed line: iso-contour of  $\tilde{c} = 0.5$

a broad laser beam (~0.5 mm) precisely. An inconsequential deviation (<0.1 mm) of the laser beam from the central plane is sufficient to produce this asymmetry, while still remaining within an acceptable range of experimental error.

The local 2D mean flame surface density,  $\Sigma_{2D}$ , is shown in Fig. 2(right), uncorrected for 3D effects (Karpetsis and Barlow 2005; Veynante et al. 2010). The figure shows only a slight asymmetry about the central line axis resulting from imperfect flow induction. Notably and as expected, the flame brush thickness estimated as the mean-variance of  $\tilde{c}$  and  $\tilde{c}$  is significantly larger at the flame tip than at the base.

A comparison between total mass flow rates (measured by mass flow controllers, MFC, 5% uncertainty),  $\dot{m}$ , and total reaction rates,  $\dot{\Omega}$ , are shown in Table 2. Total reaction rates in experiments can be estimated by assuming that flames behave as unstrained flamelets, so that the local reaction rate is  $\bar{\omega}_c = \rho_u s_L \Sigma_{2D}$ , and that the flame is symmetric about the vertical plane.

$$\dot{\Omega}_c = \int_{V_0} \bar{\omega}_c dV = \int_0^H \int_0^R 2\pi r \bar{\omega}_c dr dz = \int_0^H \int_0^R 2\pi r \rho_u s_L \Sigma_{2D} dr dz \quad (15)$$

where  $r$  and  $z$  are now the radial and axial coordinates, and  $\Sigma_{2D}$  is taken as the average value between the left and right sides of the flame.

Zheng et al. (2023) showed for the same flame that the difference between  $\Sigma_{3D}$  and  $\Sigma_{2D}$  is relatively small in the relevant regions away from the centerline. Therefore, using  $\Sigma_{2D}$  to estimate total reaction rates should lead to corrections of the order of less than 10% in this study.

### 4.2 Progress of Reaction Balance Along Streamlines

In this section, we quantify the terms in the conservation of  $\tilde{c}$  in Eqs. (3) and (6) along streamlines, based on measured experimental values, and check how well the reconstructed 2D terms are able to close the progress of reaction balance. Streamlines are derived from the mean velocity field. All experimental values along streamlines were interpolated from a 2D scalar field (pixel resolution of 39  $\mu\text{m}/\text{pixel}$ ) or 2D vector field (PIV cross-correlation with 16x16 pixel<sup>2</sup> window size). The analysis along streamlines means that it is conducted in a differential form within an infinitesimal volume with no mass crossing the control volume on the mean. However, the net flux of diffusive terms can be non-zero.

Four mean streamlines are selected for further analysis, as illustrated in Fig. 3a. Streamlines correspond to symmetric locations starting from approximately on the negative (N1, N2) or positive (P1, P2) sides of the  $r$ -axis. The low Ka on Table 1 means that the flamelet assumption can be reasonably assumed. However, the assumption would fail near the base of the flame, where the stabilization involves laminar reactions with thick reaction zones near the regions of large heat loss.

**Table 2** Comparison of total mass flow rate of reactant  $\dot{m}$  and corresponding total reaction rate  $\dot{\Omega}_c$

	$\dot{m}$ (g/min)	$\dot{\Omega}$ (g/min)	$\frac{\dot{\Omega}_c}{\dot{m}} - 1$ (%)
Case 1	16.3	15.9	- 2.8
Case 2	16.6	16.5	- 0.7

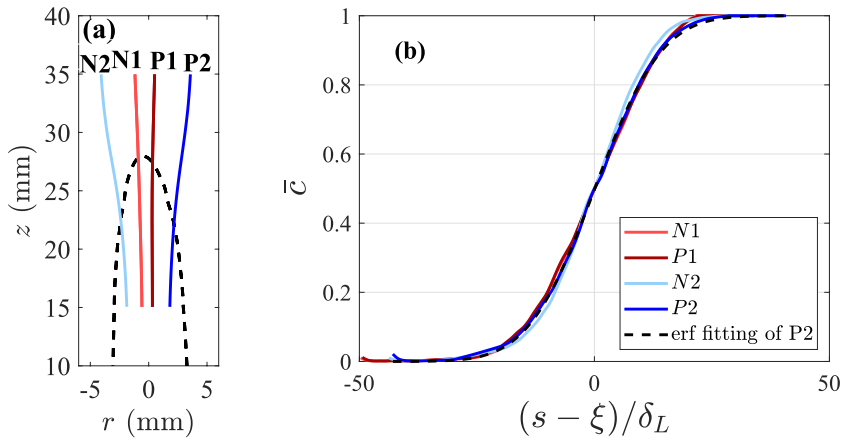


**Fig. 3** Mean progress variables along streamlines. **a** Illustration of streamlines in the negative (N) and positive (P) sides of the images for Case 1. Black solid lines start from the  $\bar{c} = 0.1$  and end at  $\bar{c} = 0.9$  where uncertainty in flame edge location leads to a slight asymmetry. **b** Profiles of  $\bar{c}$  along streamlines N1, N2, P1 and P2 for Case 1. The distance coordinate is normalized by laminar flame thickness  $\delta_L$  in Case 1. Black dashed line: a fitted curve of line P2 based on Gaussian diffusion

The procedure for the calculations is as follows: (a) the measured values of velocity and  $\bar{c}$  are interpolated from the 2D field by using *Matlab* function *interp2* along streamlines of coordinate  $(r(s), z(s))$ , (b) physically based fitting and filtering is applied in regions where differentiation is required, in order to minimize high frequency noise.

In what follows, the terms for the balance of progress of reaction are calculated, and the terms in Eq. 5 are illustrated for Case 1.

### 4.2.1 Mean Progress Variables, $\bar{c}$ and $\bar{c}$

Figure 3b shows the evolution of mean progress variables  $\bar{c}(s)$  along the selected streamlines for Case 1, along with a fitted curve based on Gaussian diffusion, denoted  $\bar{c}_1$  as follows:

$$\bar{c}_1(s) = \frac{1}{\sqrt{2\pi}\sigma} \int_{-\infty}^s \exp\left(-\frac{(s-\xi)^2}{2\sigma^2}\right) ds = \frac{1}{2} \left[ 1 + \operatorname{erf}\left(\frac{s-\xi}{\sqrt{2}\sigma}\right) \right] \tag{16}$$

where  $\xi$  is the  $s$  distance coordinate at  $\bar{c} = 0.5$ ,  $\operatorname{erf}(x) = (2/\sqrt{\pi}) \int_0^x \exp(-t^2) dt$  is the error function. The correlation coefficients  $R^2$  of the fitting function using Eq. (16) are within 1.5% of unity for all cases.

### 4.2.2 Gradients of $\bar{c}$ and $\bar{c}$

In order to reckon the convective term in the balance of  $\bar{c}$ , the magnitude and direction of the mean gradient of Favre-averaged progress of reaction,  $\nabla \bar{c}$  is necessary. The gradient of

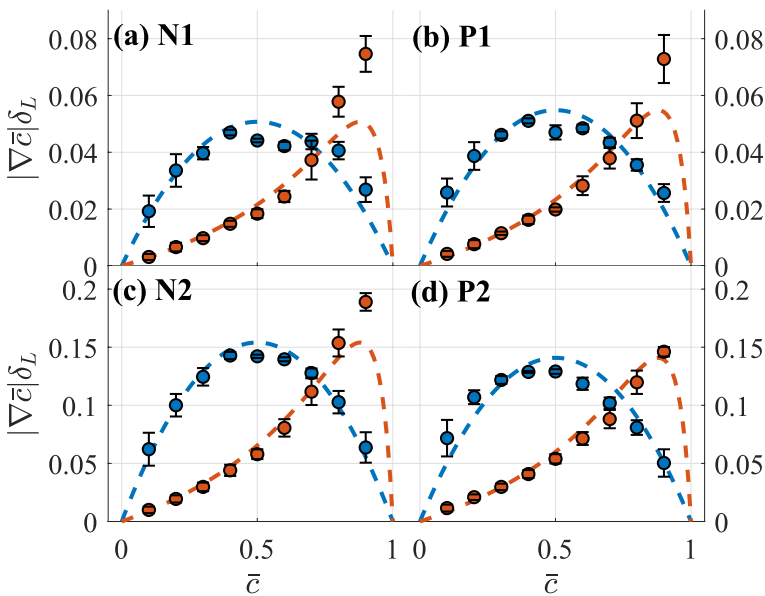
the mean variable,  $\nabla \bar{c}$ , is obtained from the fitted curves determined by Eq. (16), and  $\nabla \tilde{c}$  is obtained assuming a thin flamelet, so that:

$$\frac{|\nabla \tilde{c}|}{|\nabla \bar{c}|} = g = \frac{\rho_u \rho_b}{\bar{\rho}^2} = \frac{\Theta}{(\Theta(1 - \bar{c}) + \bar{c})^2} \tag{17}$$

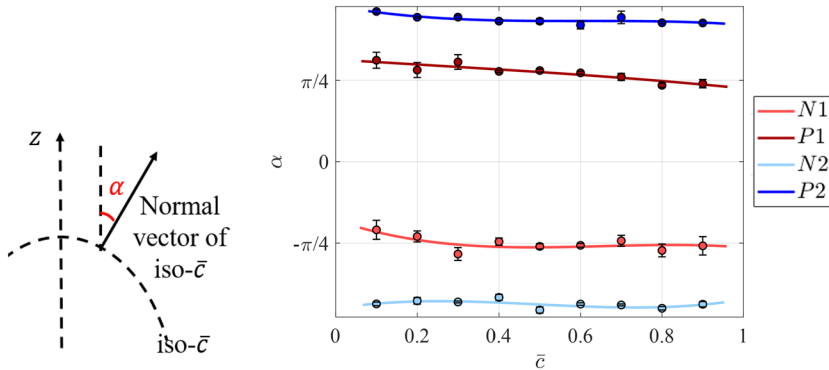
The factor  $g$  is an increasing function of  $\bar{c}$  from  $1/\Theta$  (at  $\bar{c} = 0$ ) to  $\Theta$  (at  $\bar{c} = 1$ ), and balances at  $g = 1$  at values for  $\bar{c} \approx 0.72$ . The relevance of the factor  $g$  becomes apparent further on, as uncertainties in the measurements of  $\nabla \bar{c}$  are amplified in the calculations.

Figure 4 shows the magnitude of  $\nabla \bar{c}$  and  $\nabla \tilde{c}$  along the selected streamlines, along with fitting functions, as a function of  $\bar{c}$ . The measurements are proportional to  $\bar{c}(1 - \bar{c})$ , as expected from the differentiation of cumulative Gaussian distribution. The proportionality constant  $k$  can be interpreted as  $k = \sqrt{2}/\sigma$ , where  $\sigma$  is the variance of the corresponding flamelet bimodal fluctuation [in Eq. (16)]. The values of  $|\nabla \bar{c}|$  (blue symbols) are fitted accordingly (dashed blue line), and the corresponding fit for the magnitude of  $|\nabla \tilde{c}|$  is obtained from Eq. (17). The fitted value of  $k$  is a factor of two smaller for the streamlines closer to the centerline compared to those further towards the edges. This reflects the much larger variance observed near the crest of the flame compared to the edges, as expected from the growth of the length scale from the anchoring point. Whereas the error between the fitted curve to  $\bar{c}$  is relatively small, the fitting error for  $|\nabla \tilde{c}|$  is amplified by the value of the factor  $g$ , which crosses unity around  $\bar{c} = 0.72$  and increases to  $\Theta = 7.3$  at the trailing edge (deviation between red points and red dash lines at **N1** and **P1** in Fig. 4).

Whereas the magnitude of  $\nabla \bar{c}$  changes significantly along the flame brush, the same is not true of its the directing angle  $\alpha$  shown in Fig. 5, defined as the angle between the



**Fig. 4** Values of  $|\nabla \bar{c}|$  (blue symbols) and  $|\nabla \tilde{c}|$  (red symbols) along streamlines normalized by unstrained laminar flame thickness  $\delta_L$ . Dashed blue lines correspond to fitting with the functions  $k\bar{c}(1 - \bar{c})$ , with  $k_{N1} = 0.2$ ,  $k_{P1} = 0.22$ ,  $k_{N2} = 0.616$ ,  $k_{P2} = 0.54$ . Dashed red lines correspond to  $|\nabla \tilde{c}| \delta_L$ ; with derived functions from  $|\nabla \bar{c}|$



**Fig. 5** Local direction of normal vectors  $\hat{n}$  of  $\bar{c}$ -isocontours expressed as the angle between the vector and the  $z$ -axis. Left: schematic illustration of angle  $\alpha$

normal vector of the  $\bar{c}$ -isocontour and the vertical  $z$ -axis. The angle remains approximately constant along the streamlines across the flame brush with a slight change accounting for the expansion of the flow from leading to trailing edge. We note that there is a slight flow asymmetry leading to slightly different angles on the left and right side of the flame.

### 4.2.3 Velocities $\bar{u}, \tilde{u}$

In order to reckon the different terms in the  $\tilde{c}$  balance equation along the flame brush, both the mean and fluctuating velocities are required. The value of the absolute magnitudes of the mean and Favre-averaged 2D velocities (there is negligible mean 3D component in the symmetric setup) along the selected streamlines is based on the ensemble-average and the Favre-average of local velocities, respectively, regardless of whether in the reactant side or product side, and shown in Fig. 6 (top). Figure 6 (bottom) presents conditional mean velocities at the reactant and product sides,  $\bar{u}_u$  and  $\bar{u}_b$ , determined based on the local conditional average of the measurement relatively to the binarized images, to separate reactant and product regions. Mirroring the mean velocities, these also do not change much across the flame. The flow pattern is driven primarily by the pressure gradient and the necessary divergence to accommodate expansion, and in the present case, both the acceleration and divergence are relatively small. Figure 7 presents the corresponding velocity directions, defined as the angle  $\beta$  between the velocity vector and  $z$ -axis, with a distinction made between the mean unburnt (dashed) and burned (dash-dotted) values. The measurement shows that the mean velocity magnitudes increase only slightly across the flame brush, as the streamlines diverge to accommodate the density change. Note that the mean angles corresponding to the burned gases show a systematically larger angle owing to the expansion.

### 4.2.4 Favre Correlation $\widetilde{u''c''}$ and Counter-Gradient Diffusion

The turbulent flux term  $\nabla \cdot \mathbf{T}_c^F$  in Eq. (4) requires measurement of the cross-correlation of velocity residual  $\mathbf{u}''$  and progress residual  $c''$ . In the present flamelet bimodal approximation, the cross-correlation  $\widetilde{u''c''}$  can be obtained from the conditional velocities in the reactant side and product side can be extracted from Figs. 6 and 7, shown in Eq. (7).

**Fig. 6** Top: absolute magnitudes of mean and Favre-averaged velocities along streamlines. Blue line:  $\bar{u}$ ; red line:  $\tilde{u}$ . Bottom: magnitudes of conditional mean velocities in unburnt and burnt sides, Blue lines:  $\bar{u}_u$ ; red lines:  $\bar{u}_b$

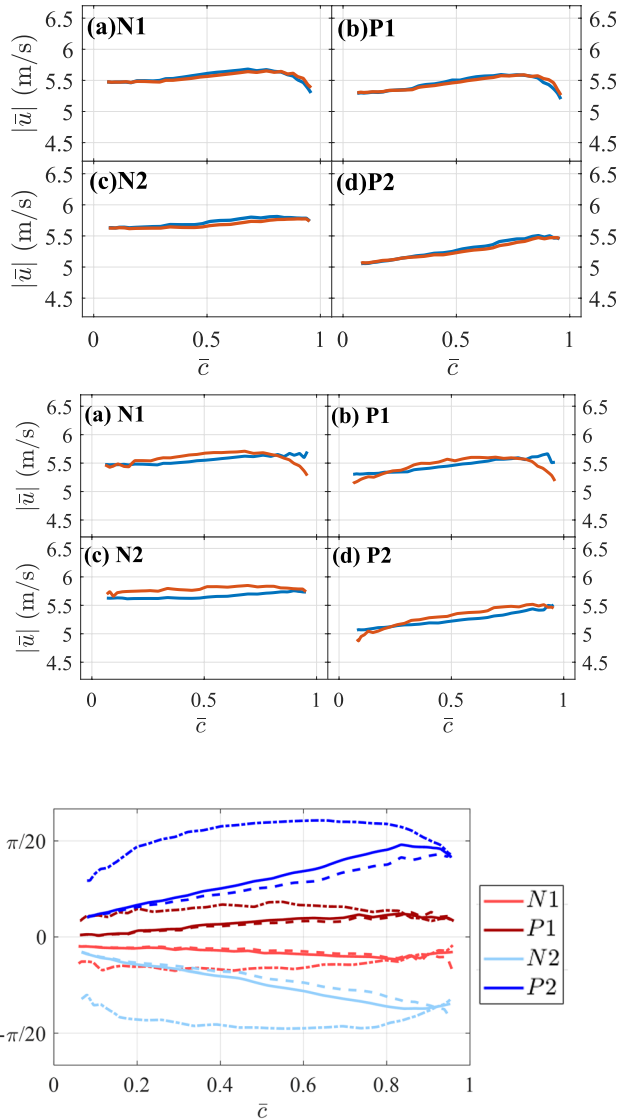


**Fig. 7** Angle  $\beta$  indicating the direction of 2D velocity vectors along streamlines relatively to axial/vertical axis. Solid lines:  $\bar{u}$ ; dashed line:  $\bar{u}_u$ ; dash-dotted line:  $\bar{u}_b$ . Left: schematic illustration of angle  $\beta$  as tangent to streamlines

When evaluating the value of  $\widetilde{\mathbf{u}''c''}$ , it is useful to consider alternative formulations of Eq. (7) which can minimise uncertainties in the determination of the gradient of  $\bar{c}$ : the value of  $\bar{u}_u$  is more accurate in the range of  $\bar{c} = 0$  to 0.5, whereas the value of  $\bar{u}_b$  is more accurately determined over  $\bar{c} = 0.5$  to 1. One can therefore reformulate Eqs. (18)–(19) by using either  $\bar{u}_b$  or  $\bar{u}_u$ , respectively:

$$\overline{\rho \mathbf{u}'' c''} = \rho_b \overline{\mathbf{u}_b c} - \overline{\rho \mathbf{u} c} = \rho_b \overline{c} (\overline{\mathbf{u}_b} - \overline{\mathbf{u}}) \tag{18}$$

$$= \overline{\rho \mathbf{u}} (1 - \overline{c}) - \rho_u \overline{\mathbf{u}_u} (1 - \overline{c}) = \rho_u (1 - \overline{c}) (\overline{\mathbf{u}} - \overline{\mathbf{u}_u}) \tag{19}$$

In a steady planar turbulent flame,  $\overline{\mathbf{u}_b} - \overline{\mathbf{u}_u}$  is larger than 0 and therefore,  $\overline{\mathbf{u}'' c''} > 0$ . This is in the opposite direction of gradient transport of  $\overline{c}$  (gradient diffusion) (Peters 2000), and counter-gradient diffusion (Libby and Bray 1981), a topic which has been discussed in many previous papers (Libby and Bray 1981; Libby and Williams 1994; Bray 2005).

Once the flux term is calculated, one can consider whether the diffusive flux  $\overline{\mathbf{u}'' c''}$  points in the same or opposite direction to that of  $\nabla \overline{c}$ . The angle  $\alpha''$ , which determines the direction of  $\mathbf{u}'' c''$ , is determined as the angle between the  $z$ -axis and  $\mathbf{u}'' c''$  obtained from Eq. (19) at  $0 < \overline{c} < 0.5$  and Eq. (18) at  $0.5 < \overline{c} < 1$ .

The direction of diffusion is obtained by comparing the angle difference between  $\overline{\mathbf{u}'' c''}$  and  $\nabla \overline{c}$ , illustrated by the absolute value of  $|\alpha - \alpha''|$ : values close to zero (parallel in the same direction) indicate counter-gradient diffusion, whereas values close to  $\pi$  (parallel in the opposite direction) are indicative of gradient diffusion.

Figure 8 shows the value of the magnitude of the diffusion flux (left) normalized by the laminar flame speed. The values are very small for the cases (N1, P1 closer to the centerline) from the leading edge up to nearly the trailing edge, where they turn negative (gradient diffusion). In contrast, for the cases away from the centerline (N2, P2), the fluxes increase slightly in the counter-gradient direction, up to the trailing edge, where gradient diffusion takes over. The conclusion is corroborated by the value of the angle difference  $|\alpha - \alpha''|$  between the vector of  $\mathbf{u}'' c''$  and  $\nabla \overline{c}$  along the streamlines. In the range of  $0 < \overline{c} < 0.8$ , the angle difference of two vectors is small, and  $\overline{\mathbf{u}'' c''}$  and  $\nabla \overline{c}$  both point in a similar direction. Therefore, counter-gradient diffusion effects play a dominant role at the leading edge and the middle of the flame brush. Nearer the trailing edge ( $0.8 < \overline{c}$  in P1 and N1 and  $0.9 < \overline{c}$  in P2 and N2), the angle difference between the two vectors jump to values close to  $\pi$ , and two vectors are in opposite directions, which means the counter-gradient diffusion turns into gradient diffusion (Kalt et al. 1998; Troiani et al. 2013; Kheirkhah and Gülder 2015).

More importantly, the sudden increase in the angle difference in Fig. 8 shows that the transition from the counter-gradient diffusion to the gradient diffusion occurs over

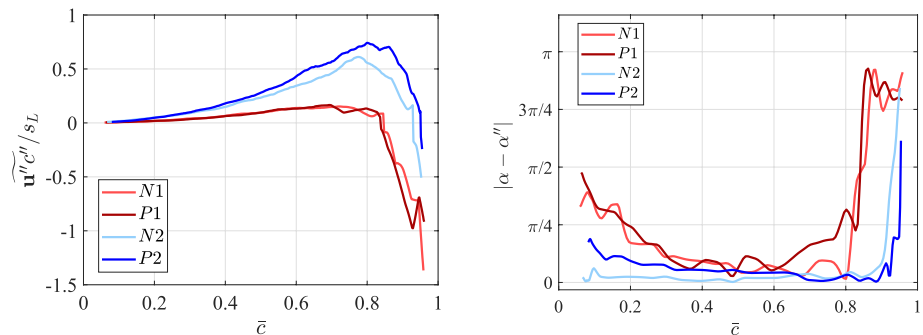


**Fig. 8** Magnitude and direction of Favre correlation  $\overline{\mathbf{u}'' c''}$  from Eq. (7). Left: Magnitude normalized by  $s_L$ , minus value corresponds to inverse direction between  $\mathbf{u}'' c''$  and  $\nabla \overline{c}$ ; Right: Angle difference between the Favre correlation and  $\nabla \overline{c}$  along streamlines

a very narrow spatial region, so that the probability of finding turbulent fluxes normal to  $\nabla\bar{c}$  is low. In those circumstances, it may be reasonable to model the turbulent flux  $\overline{\mathbf{u}''c''}$  as a linear function of  $\nabla\bar{c}$  with a linear factor, while the sign of the linear factor depends on whether there is counter or gradient diffusion. By comparing Figs. 4 and 8a, this factor is found to be of the order of  $2s_L\delta_L$  at  $\bar{c} = 0.5$ , increasing towards the reactant side.

### 4.2.5 Divergence of Turbulent Flux $\nabla \cdot (\overline{\rho\mathbf{u}''c''})$

Once the diffusion flux term is determined, its divergence can be calculated. The accuracy of the divergence term  $\mathbf{T}_c^F$  can be improved by considering alternative formulations of Eq. (7) with Eqs. (18) and (19). In the calculation of the divergence of  $\mathbf{T}_c^F$  close to the leading edge ( $0 < \bar{c} < 0.5$ ), Eq. (19) is employed to avoid the use of the less accurate  $\bar{\mathbf{u}}_b$  in that range.

$$\nabla \cdot (\overline{\rho\mathbf{u}''c''})|_u = \rho_u(1 - \bar{c})(\nabla \cdot \bar{\mathbf{u}} - \nabla \cdot \bar{\mathbf{u}}_u) - \rho_u(\bar{\mathbf{u}} - \bar{\mathbf{u}}_u) \cdot \nabla\bar{c} \tag{20}$$

Conversely, close to the trailing edge ( $0.5 < \bar{c} < 1$ ), Eq. (18) is applied to avoid  $\bar{\mathbf{u}}_u$ .

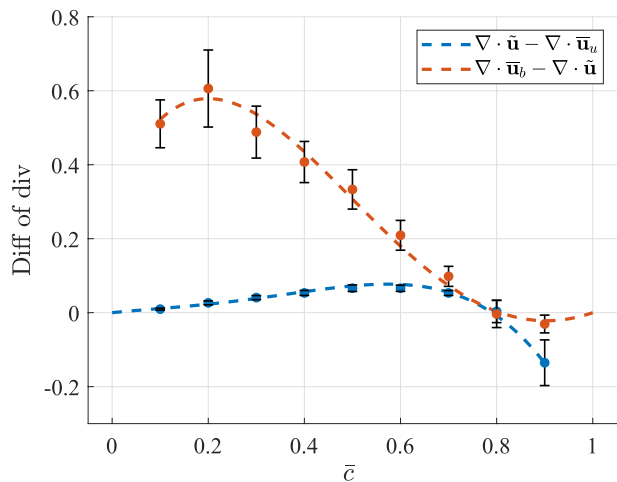
$$\nabla \cdot (\overline{\rho\mathbf{u}''c''})_b = \rho_b\bar{c}(\nabla \cdot \bar{\mathbf{u}}_b - \nabla \cdot \bar{\mathbf{u}}) + \rho_b(\bar{\mathbf{u}}_b - \bar{\mathbf{u}}) \cdot \nabla\bar{c} \tag{21}$$

At both the leading and trailing edge, the divergence of  $\overline{\mathbf{u}''c''}$  is equal to zero, and the difference of velocity divergence,  $\nabla \cdot \bar{\mathbf{u}} - \nabla \cdot \bar{\mathbf{u}}_u$  and  $\nabla \cdot \bar{\mathbf{u}}_b - \nabla \cdot \bar{\mathbf{u}}$ , are also zero. Therefore, any fitting curve for the sum of terms should pass through zero at the limits  $\bar{c} = 0$  and  $\bar{c} = 1$ .

Figure 9 shows the terms involving the difference in velocity divergence for the case of N1. The corresponding first terms in Eqs. 20 and 21 are approximated using third-order polynomial functions.

For the second term in Eq. 21 involving the inner product of the velocity difference and the gradient of  $\bar{c}$ , the calculation was converted into a product of the absolute magnitude of the terms times the cosine of the corresponding angles between the

**Fig. 9** Difference in velocity divergence terms in Eqs. (20) and (21) along N1 normalized by  $s_L/\delta_L$ , along with fitted 3rd order polynomial curves





normal each  $\bar{c}$ -isocontour and velocity vector. The latter is determined by determining and fitting the angle difference between the velocity and normal vector of  $\bar{c}$ -isocontour.

$$\begin{aligned}
 -\rho_u(\bar{\mathbf{u}} - \bar{\mathbf{u}}_u) \cdot \nabla \bar{c} &= -\rho_u |\nabla \bar{c}| (\bar{\mathbf{u}} \cdot \hat{\mathbf{n}} - \bar{\mathbf{u}}_u \cdot \hat{\mathbf{n}}) \\
 &= -\rho_u |\nabla \bar{c}| (|\bar{\mathbf{u}}_u| \cos(\alpha - \beta_u) - |\bar{\mathbf{u}}| \cos(\alpha - \beta))
 \end{aligned}
 \tag{22}$$

$$\begin{aligned}
 \rho_b(\bar{\mathbf{u}}_b - \bar{\mathbf{u}}) \cdot \nabla \bar{c} &= \rho_b |\nabla \bar{c}| (\bar{\mathbf{u}}_b \cdot \hat{\mathbf{n}} - \bar{\mathbf{u}} \cdot \hat{\mathbf{n}}) \\
 &= \rho_b |\nabla \bar{c}| (|\bar{\mathbf{u}}_b| \cos(\alpha - \beta_b) - |\bar{\mathbf{u}}| \cos(\alpha - \beta))
 \end{aligned}
 \tag{23}$$

Through invoking Eqs. (22) and (23) into Eqs. (20) and (21), and extracting the difference of divergence from Fig. 9, the turbulent flux term can be derived in the  $0 < \bar{c} < 0.5$  and  $0.5 < \bar{c} < 1$  respectively, with a linear combination of the two expressions created to avoid discontinuity  $\bar{c} = 0.5$  for the final turbulent flux,  $\nabla \cdot (\bar{\rho} \bar{\mathbf{u}}'' c'') = (1 - \bar{c}) \nabla \cdot (\bar{\rho} \bar{\mathbf{u}}'' c'')|_u + \bar{c} \nabla \cdot (\bar{\rho} \bar{\mathbf{u}}'' c'')|_b$ .

Figure 10 shows the final divergence of turbulent fluxes along streamlines, with error bars representing the uncertainty using error propagation. Velocity magnitudes and velocity angles used for fitting the red dashed lines are derived from Figs. 6, 5 and 7 with third-order polynomials. Values of gradient  $|\nabla \bar{c}|$  used for fitting the red dashed line are derived from Fig. 4 using a parabolic equation.

### 4.2.6 Flame Surface Density

One of the possible ways of estimating the local mean reaction rate  $\bar{\omega}_c$  for low turbulence flames in the flamelet regime is to measure the local flame surface density, with the assumption that

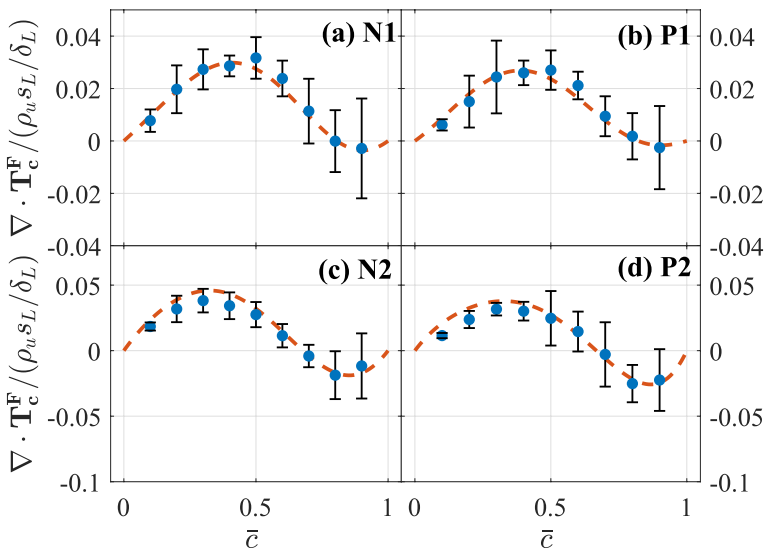


**Fig. 10** Divergence of the turbulent flux  $\nabla \cdot \mathbf{T}_c^F$  normalized by  $\rho_u s_L / \delta_L$ . Symbol: conditional average of measured  $\mathbf{T}_c^F$ ; red dash line: fitted  $\mathbf{T}_c^F$  derived from Eqs. (20) and (21)

$$\bar{\omega}_c = \rho_u s_L \Sigma_{2D} = \rho_u s_L |\overline{\nabla c \delta(c - c^*)}| \tag{24}$$

where  $\Sigma_{2D}$  is determined as in Eq. (11). Two objections might be raised in these estimates: (a) the identity ignores the role of stretch on the local flame speed, and (b) the flame surface density must be measured in 3D. Regarding (a), the purpose of the present exercise is not to propose a model for the stretch factor, but instead to see how the simple analysis fares. Regarding (b), we note that recent measurements of FSD by Zheng et al. (2023) in the same setup showed that 3D FSD measurements are higher than 2D estimates by 10–30%, and that this must be kept in mind when considering discrepancies. Measurements of  $\Sigma_{2D}$  along the selected streamlines are shown in Fig. 11, as an average of 4000 images. Local fluctuations in the measurements arise from the limited pixel resolution of  $39 \mu\text{m}/\text{pixel}$ , which creates noise when local gradients are reckoned. The FSD is proportional to the variance of  $c$  via the probability of presence of flame edges [see Eq. (11)], so that the measurements are found to be proportional to  $\bar{c}(1 - \bar{c})$ , in the same manner as  $|\nabla \bar{c}|$  in Fig. 4. Notice that  $|\nabla c|$  is not equal to  $|\nabla \bar{c}|$ . The latter is shown in Fig. 4, and represents the magnitude of the gradient of the mean  $\bar{c}$ , whereas the former is the mean product of the probability of finding flame edges times the local mean.

### 4.3 Favre-Averaged Progress Variable Conservation

Now that the components of the terms in the balance equation Eq. (5) have been determined, one can compare the turbulent displacement speed,  $s_T$ , on the LHS, to the sum of the magnitudes of the components  $s_F, s_R, s_D$  (in *Supplementary material* Appendix A) corresponding to the reaction, molecular diffusive term and turbulent flux terms on the RHS.

A fidelity check of the mass conservation along the flame was conducted by considering the difference between the total measured flow rate and the integrated mass flow rate at the

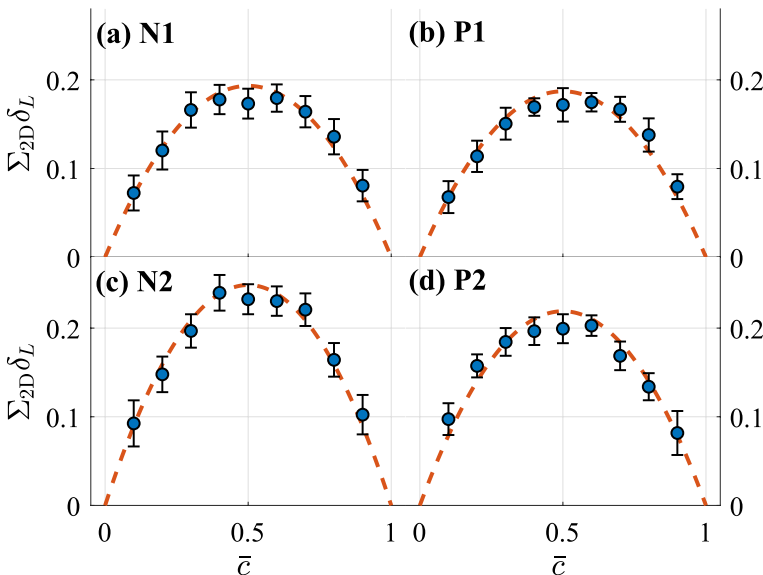


Fig. 11 Mean 2D flame surface density measurements along the indicated streamlines

leading edge,  $\int_{A_0} \rho_0 \tilde{\mathbf{u}}_0 \cdot \hat{\mathbf{n}} dA$ , which was found to be 10–15% lower than the measured flow rate. The validation of mass conservation in the extended downstream region of the flame brush cannot be completely verified owing to potential entrainment of the unseeded pilot flow. Considering individual streamtubes from leading to trailing edge, the agreement is somewhat less favorable, and within within  $\pm 30\%$ . The discrepancy can be primarily attributed to the uncertainty associated with estimating the angle difference  $|\alpha - \beta|$  in the regions upstream of the flame. Further details are available in “Appendix”.

### 4.3.1 Local Displacement Speed $s_T$

The local displacement speed  $s_T$  in a statistically stationary flame is equal to the Favre-averaged velocity normal to the  $\bar{c}$ -isosurface,  $\tilde{\mathbf{u}} \cdot \hat{\mathbf{n}}$ . By assuming Bunsen flames to be circumferentially symmetrical, the normal vector of  $\bar{c}$ -isosurface coincides with the normal vector of  $\bar{c}$ -isocontour in 2D measurement. The inner product between velocity vectors and the normal vector of  $\bar{c}$ -contour is expressed as the product of velocity magnitude and the cosine of  $\alpha - \beta$ , which is fitted by a polynomial to reduce the error of the normal vector of  $\bar{c}$ -isocontour.

$$s_T = \tilde{\mathbf{u}} \cdot \hat{\mathbf{n}} = |\tilde{\mathbf{u}}| \cos(\alpha - \beta) \tag{25}$$

Figure 12 presents measured values of  $s_T = |\tilde{\mathbf{u}}| \cos(\alpha - \beta)$  (red dashed line) and  $s_T = \tilde{\mathbf{u}} \cdot \hat{\mathbf{n}}$  (blue symbols). The red dashed lines, corresponding to the same measurements, where angle difference  $\alpha - \beta$  is fitted by a 3rd order polynomial as a function of  $\bar{c}$  respectively based on Figs. 5 and 7. The main difference between  $\tilde{\mathbf{u}} \cdot \hat{\mathbf{n}}$  and  $|\tilde{\mathbf{u}}| \cos(\alpha - \beta)$  comes from the noise of the normal vector  $\hat{\mathbf{n}}$ , which depends on the number of images and the pixel

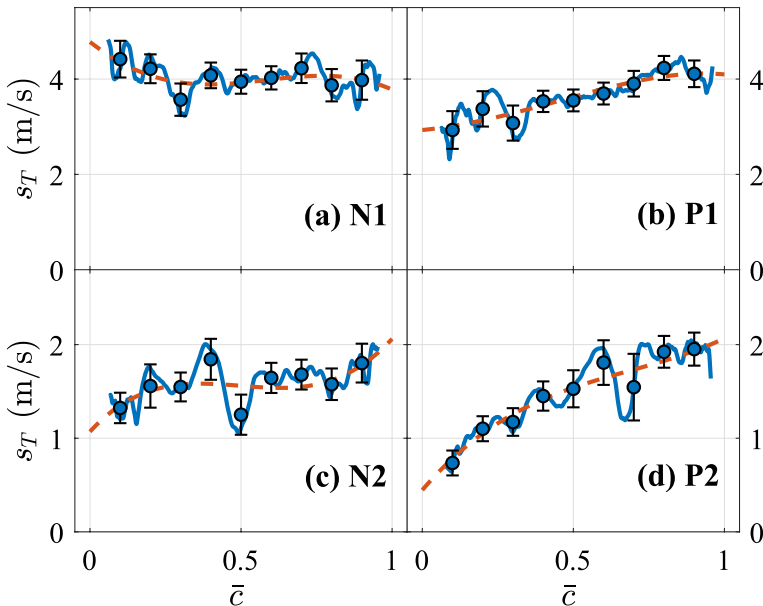


**Fig. 12** Blue symbols: measured magnitude of local displacement speed  $s_T$ . Red dashed line: measured  $s_T$  using fitted curve for  $\cos(\alpha - \beta)$ . Blue lines are a moving average

resolution. Whereas in principle collection of larger samples can reduce the uncertainty in  $\nabla\bar{c}$ , the final variance is already converged and limited by the pixel resolution.

The error bar represented in Fig. 12 corresponds to the uncertainty in both magnitudes of  $|\bar{\mathbf{u}}|$  and  $\cos(\alpha - \beta)$ , and is calculated by the propagation of uncertainty, where we currently neglect any covariance of velocity magnitudes and angles. There is clearly a difference between symmetric locations of streamlines, which may affect the accuracy of  $s_T$  by underestimating the residual of normal velocity on the third component, while the asymmetry cannot be fully removed and accounted for in the accuracy estimation. Nevertheless, the uncertainty from asymmetry on the estimation of  $s_T$  should not affect the fidelity of  $s_T$  here since it is analysed locally without considering the circumferential isotropicity of the streamtube area.

### 4.3.2 Turbulent Flux Term $s_F$

The turbulent flux velocity term  $s_F$  in Eq. (5) is calculated from the divergence of the flux,  $s_F = (1/\bar{\rho}|\nabla\bar{c}|)\nabla \cdot \overline{\mathbf{u}''c''}$ . For better accuracy, as described in Sec. 4.2.5, the divergence and the resulting flame speed is calculated over two overlapping domains below and above  $\bar{c} = 0.5$ , as  $s_{F,u}$  and  $s_{F,b}$ , respectively, as summarized in Eqs. (20) and (21). The terms are reproduced for completeness as follows:

$$s_{F,u} = \underbrace{-\frac{\bar{\rho}}{\rho_b|\nabla\bar{c}|}(1 - \bar{c})(\nabla \cdot \bar{\mathbf{u}} - \nabla \cdot \bar{\mathbf{u}}_u)}_{\text{Difference of velocity divergence}} + \underbrace{\frac{\bar{\rho}}{\rho_b}|\bar{\mathbf{u}}|\cos(\alpha - \beta) - \frac{\bar{\rho}}{\rho_b}|\bar{\mathbf{u}}_u|\cos(\alpha - \beta_u)}_{\text{Difference of normal velocity}} \tag{26}$$

$$s_{F,b} = \underbrace{-\frac{\bar{\rho}}{\rho_u|\nabla\bar{c}|}\bar{c}(\nabla \cdot \bar{\mathbf{u}}_b - \nabla \cdot \bar{\mathbf{u}})}_{\text{Difference of velocity divergence}} + \underbrace{\frac{\bar{\rho}}{\rho_u}|\bar{\mathbf{u}}|\cos(\alpha - \beta) - \frac{\bar{\rho}}{\rho_u}|\bar{\mathbf{u}}_b|\cos(\alpha - \beta_b)}_{\text{Difference of normal velocity}} \tag{27}$$

Figure 13 shows values of measured  $s_F$  and fitted  $s_F$  using Eqs. (26) and (27). In the first term of Eq. (26),  $|\nabla\bar{c}|$  is decomposed as  $k\bar{c}(1 - \bar{c})$  and  $\nabla \cdot \bar{\mathbf{u}} - \nabla \cdot \bar{\mathbf{u}}_b$  is thus fitted by  $\bar{c}(a\bar{c}^3 + b\bar{c}^2 + c\bar{c} + d)$ , leading to a cancellation of  $\bar{c}(1 - \bar{c})$ . In this case, the first term can be simplified as  $-(\bar{\rho}/\rho_b k)(a\bar{c}^3 + b\bar{c}^2 + c\bar{c} + d)$  to eliminate the singularity at  $\bar{c} = 0$ . A similar process is used for the first term in Eq. (27) for the same reason.

When values of  $s_{F,u}$  and  $s_{F,b}$  are fitted by  $\bar{c}$  separately, values of  $s_{F,u}$  and  $s_{F,b}$  are very close in the middle of the flame brush but contain small difference at both leading ( $0 < \bar{c} < 0.1$ ) and trailing edge ( $0.9 < \bar{c} < 1$ ). The difference depends on the seeding and PIV post-processing. A well-tuned seeding and much more images may resolve this issue. In the following analysis, the two approximations are linearly combined as  $s_F = (1 - \bar{c})s_{F,u} + \bar{c}s_{F,b}$ . The physically-based equation for the fitted curve in Fig. 13 is consistent with the direct measurement in most locations of the flame brush, but there are still discrepancies at the leading edge in streamlines N1 and P2. This deviation comes from the error of fitting  $\nabla\bar{c}$  with  $k\bar{c}(1 - \bar{c})$  at the leading edge. Figure 4 shows that modelling  $|\nabla\bar{c}|$  using  $\bar{c}(1 - \bar{c})$  along streamlines results in a certain discrepancy between measured values and fitted results.

The error bars shown in Fig. 13 are estimated and calculated from the uncertainty propagation of the measured terms. The uncertainty of the first term of divergence difference in Eqs. (26)–(27) is calculated based on the uncertainty of the divergence difference in Fig. 9 and the uncertainty of  $|\nabla\bar{c}|$  in Fig. 4. The uncertainty of the second and

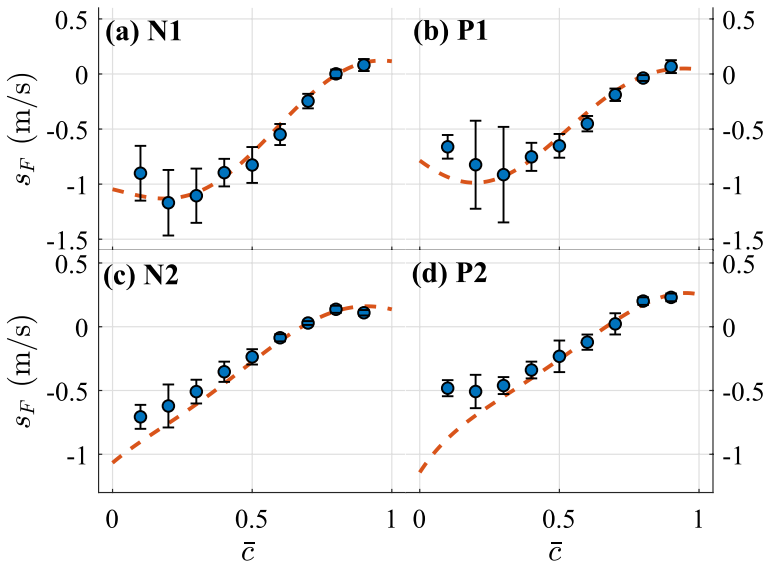


**Fig. 13** Turbulent flux velocity component of the  $\bar{c}$  balance,  $s_F$  along streamlines. Blue lines: values measured red dashed line:  $s_F$  fitted according to Eqs. (26) and (27)

third terms in Eqs. (26)–(27) are estimated to be similar to  $s_T$ , and the covariances between the second and third term are also evaluated from measurements, as there is a degree of correlation between  $\bar{\mathbf{u}}$  and conditional velocities. The total uncertainties in  $s_{F,u}$  and  $s_{F,b}$  are calculated by the uncertainty of the difference of the velocity divergence and the difference of normal velocity in Eqs. (26)–(27) based on the uncertainty propagation.

### 4.3.3 Reaction Rate Term $s_R$

The present approach aims to test the ability of the equations to close the flamelet model, using the BML assumptions, whereby the reaction rate is assumed to be proportional to the flame surface density and the laminar flame speed.

Figures 4 and 11 show that both  $|\nabla\bar{c}|$  and  $\bar{\Sigma}$  can be approximated by parabolic functions of the form  $k\bar{c}(1 - \bar{c})$ , and that the reaction term of the velocity can be rewritten as

$$s_R = s_L \Theta \left( 1 - (1 - \frac{1}{\Theta})\bar{c} \right) \frac{k_{\Sigma}}{k_{|\nabla\bar{c}|}} \tag{28}$$

where  $k_{\Sigma}$  and  $k_{|\nabla\bar{c}|}$  are constants obtained from the experimental results. Equation (28) shows that  $s_R$  should decrease linearly across the flame brush from the leading edge to the trailing edge.

The good agreement is clearly seen in Fig. 14, with some deviation near the leading edge, which arises from the deviation of  $|\nabla\bar{c}|$  to  $k_{|\nabla\bar{c}|}\bar{c}(1 - \bar{c})$  in Fig. 4. In the following analysis, a third order polynomial (black dashed line) is used for extrapolation to  $s_R$  towards  $\bar{c} = 0$ , since the red dashed line appears to overestimate the measured value of  $s_R$  at  $\bar{c} = 0$ . The uncertainty in  $s_R$  represented by the error bars was also derived from uncertainty propagation. The covariance  $\sigma_{\Sigma|\nabla\bar{c}}$  between  $\Sigma$  and  $|\nabla\bar{c}|$  is also considered here as it was not

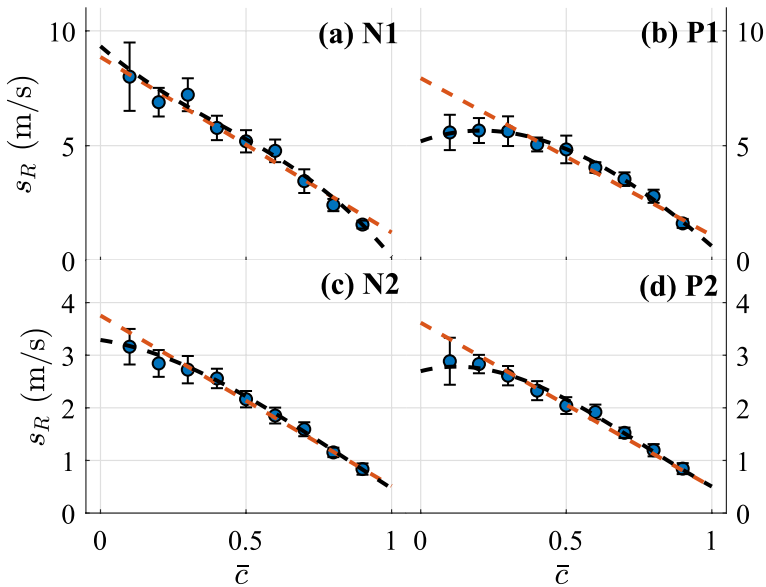


**Fig. 14** Measured reaction term  $s_T$  (blue circles) as a function of location in the flame brush along stream-line. Red dashed line: fitted  $s_R$  as Eq. (28); black dashed line: fitted to experimental datapoints curve with 3<sup>rd</sup>-order polynomials

negligible. Again, the asymmetry still exists between symmetry locations in  $s_R$  while it also does not affect the fidelity of  $s_R$  since FSD is measured locally.

#### 4.4 Testing the Balance: $s_T = s_F + s_R$

We have finally reached the point where the original identity for the balance of  $\bar{c}$ , Eq. (5), can be verified (or not) for the selected streamlines. The relevant terms in Figs. 12, 13 and 14 show absolute values of different terms in both sides of Eq. (5). Figures 15 and 16 compare the magnitude of the different terms normalized by the unstretched laminar burning velocities  $s_L$  under lean (Case 1) and rich conditions (Case 2). Solid symbols are locally measured averaged terms, and crosses (×) are extrapolated values of each term at the leading edge ( $\bar{c} = 0$ ). Blue *solid* points are local displacement speed on the LHS side of Eq. (5) and blue *open* points are the sum of  $s_F$ ,  $s_R$  on the RHS side of Eq. (5). The magnitude of  $s_D$  has been discussed in *Supplementary material* Appendix A, where it is shown that  $s_D$  can be neglected in this experiment.

Solid lines are fitted values obtained using the procedures discussed in previous discussions. Transparent areas with different colours represent uncertainties for each term. Uncertainties of burning velocities at the leading edge and the trailing edge are extrapolated by fitting uncertainties between  $0.1 < \bar{c} < 0.9$  with a third-order polynomial of  $\bar{c}$ .

The measurements in both cases show that (a) the leading order terms in the conservation equation are the reaction and convection term, with the flux term as a third component, (b) the molecular diffusion term is generally negligible, (c) the sum of reaction and diffusion terms (open blue symbols) generally overestimates the displacement speed for  $\bar{c}$  smaller than about 0.7~0.8 and underestimates it for larger values. Unsurprisingly,

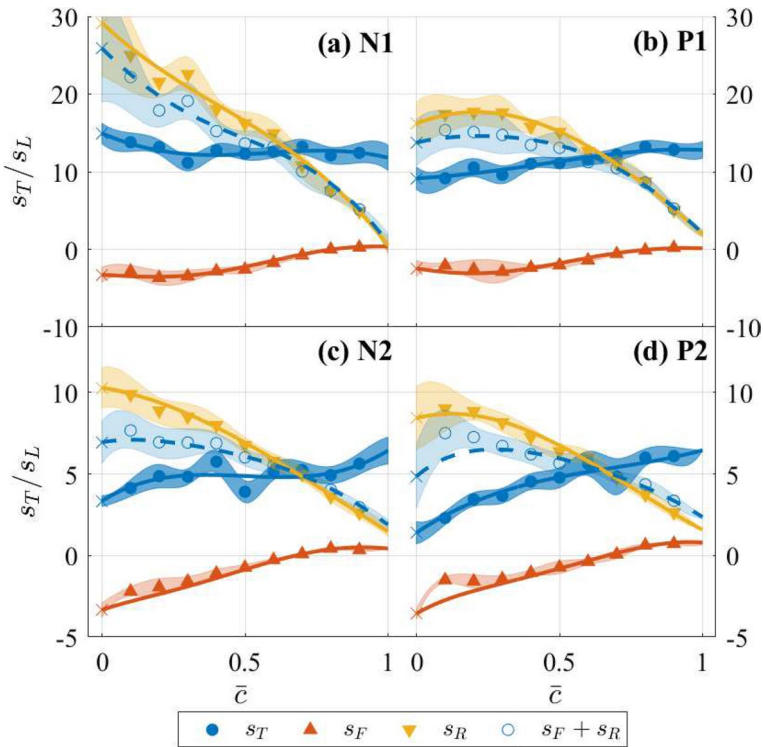


**Fig. 15** Comparison of different terms in the closure of the balance of mean progress of reaction [Eq. (5)] along streamlines in Case 1 with  $\phi = 0.9$

DNS results from Dunstan et al. (2011) at a similar turbulence level also showed the leading order terms to be reaction and convection terms for a low turbulence V-flame with  $u'/s_L = 1$ . A gradual increase in the displacement speed  $s_T$  was observed across the flame brush, and a transition in the turbulent flux speed  $s_F$  from negative to positive values at about  $\bar{c} \approx 0.7$ . However, the reaction speed  $s_R$  shows a contrasting behavior to the present values, showing an increasing trend towards the trailing edge instead of the observed decrease.

We conclude that whereas it is possible to extract displacement speeds and turbulent burning rates at the leading edge of Bunsen flames at different locations, it is particularly challenging to try to close the balance with perfect accuracy using the reaction and diffusion terms using the present techniques, which are limited in spatial accuracy. Nevertheless, one can observe fortuitous agreement in the region around  $\bar{c} \sim 0.8$ , but further investigations are needed to understand whether other factors can compensate over- or underestimation of terms. It is possible that more accurate outcomes might be obtained in flames where the streamlines cross the flame at a more favourable angle, such as opposed flames. However, the latter are not envelope flames, so it is harder to check for overall mass balance.

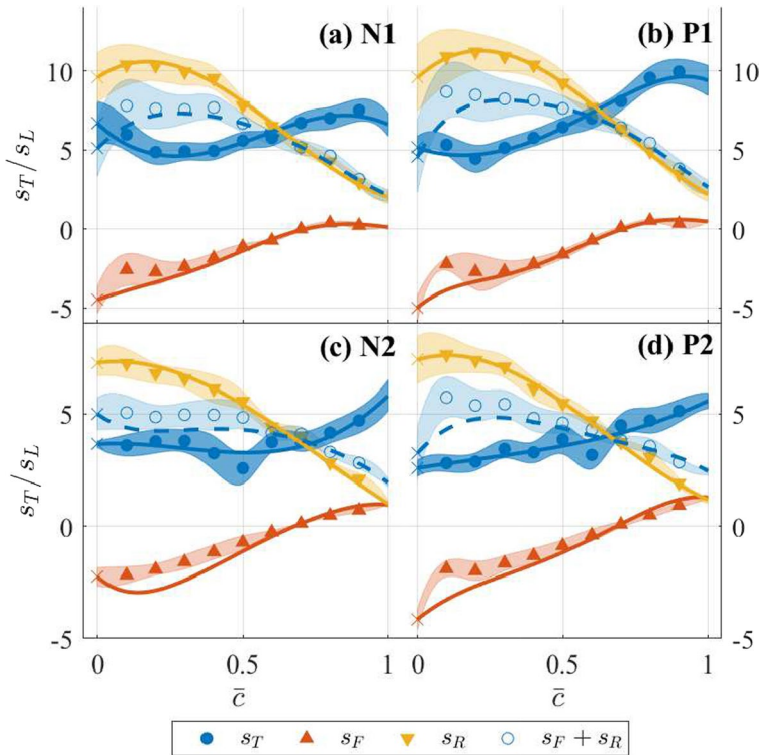


**Fig. 16** Comparison of different terms in the closure of the balance of mean progress of reaction [Eq. (5)] along streamlines in Case 2 with  $\phi = 1.2$

#### 4.5 Effect of Spatial Filtering on the Estimates of $\Sigma$ , and Inverse Filter Corrections for $s_R$

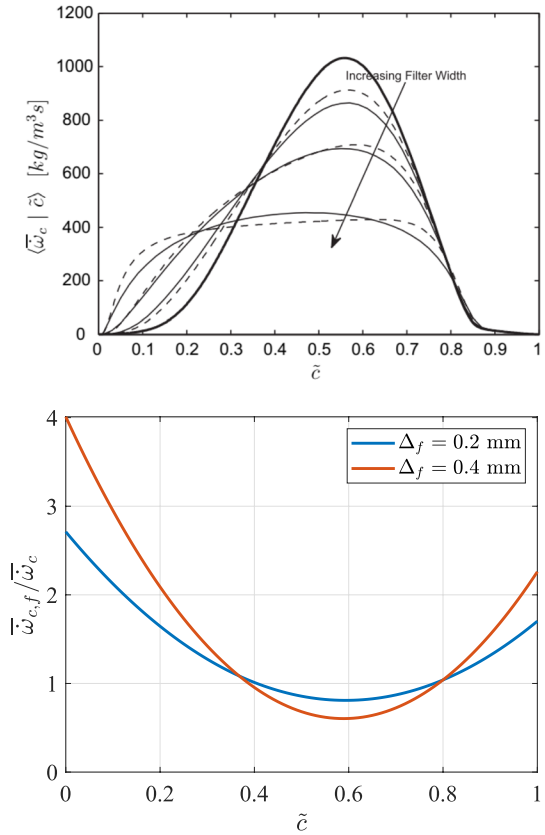
Figures 15 and 16 show a discrepancy between the convected mass flow ( $s_T$ ) into streamtubes and the resulting transported fluxes and reacting rates ( $s_F + s_R$ ). The estimated uncertainties associated with the measurements of the fluxes have been discussed above and incorporated in the form of indicated areas. The final source of uncertainty remaining is the modelled value of  $s_R$ , as well as the approximation of  $\Sigma_{2D}$  rather than its 3D counterpart, which is currently not accessible.

One possible error source is the finite spatial resolution of the present measurements, estimated as the order of  $\sim \delta_L/2 \approx 0.25$  mm (Sect. 3.3). One approach to correct for the spatial filtering of the FSD average filtered  $\Sigma$  is to estimate a correction factor corresponding to the ratio of the *actual* mean reaction to the *filtered* mean reaction rate, so that the value of  $s_R$  can be inversely corrected to the corresponding actual mean reaction rate.

Mukhopadhyay et al. (2015) performed DNS studies in slot premixed flames of stoichiometric CH<sub>4</sub>/air at turbulent conditions of  $Ka = 73$  and  $Re_\lambda = 60$  (higher than cases in Table 1) in decaying turbulence, and considered the role of a spatial filter in the development of LES submodels. Such considerations have also been made by Vreman et al. (2009) and Moureau et al. (2011) in the context of LES subgrid models. In the work of



**Fig. 17** Upper: reprint from Mukhopadhyay et al. (2015) Top: results of the filtered source term (thin solid lines) obtained by convolving DNS results with a 3D top-hat filter of width  $\delta = 0.2, 0.4, 0.8$  mm and the unfiltered source term (thick solid line) shown as a function of mean progress variable. Bottom: ratio of local conditional filtered mean reaction rate to the unfiltered value,  $\bar{\omega}_{c,f}/\bar{\omega}_c$  from DNS results, for different filter sizes



Mukhopadhyay et al. (2015), the resulting local volumetric reaction rate for the progress of the reaction was filtered with spatial filters of different sizes, and compared to the original DNS values. Figure 17 shows the results of the study extracted from Fig. 6 in Mukhopadhyay et al. (2015) in the form of the ratio of filtered mean reaction rate  $\bar{\omega}_{c,f}$  to the DNS mean reaction rate  $\bar{\omega}_c$  as a function of  $\bar{c}$  for the two different filter sizes used ( $\delta_L = 0.512$  mm). The results show that the ratio  $\bar{\omega}_{c,f}/\bar{\omega}_c$  depends both on  $\bar{c}$  as well as the filter size.

A hypothesis is therefore that one could correct the modelled value of  $s_R$  by the calculated factor  $\bar{\omega}_{c,f}/\bar{\omega}_c$  in Fig. 17. Although the numerical  $Ka$  is higher than experimental cases,  $Re$  is of the same order. One can use Fig. 17 to estimate the possible effect of the inverse correction. The following inverse correction can show how spatial filtering might have affected the measurements.

The values of  $s_R$  were corrected by the estimated filtering correction factor, assuming the estimated filter size of  $\Delta_f = 0.2$  mm in Fig. 17 where the filter-to-thickness ratio  $\Delta_f/\delta_L = 0.4$  is close to the estimated ratio  $\Delta_f/\delta_L$  of the order of 0.5 in this study. Figure 18 presents the corrected burning velocities  $s_{R,c}$  and the sum of  $s_{R,c} + s_F$ .

Once the correction is applied, the sum  $s_{R,c} + s_F$  (open blue circles) shows a closer agreement with  $s_T$  (solid blue circles) in Fig. 18 for  $0 < \bar{c} < 0.9$ , in contrast with the significant discrepancies in Figs. 15 and 16. The discrepancy between  $s_T$  and the sum

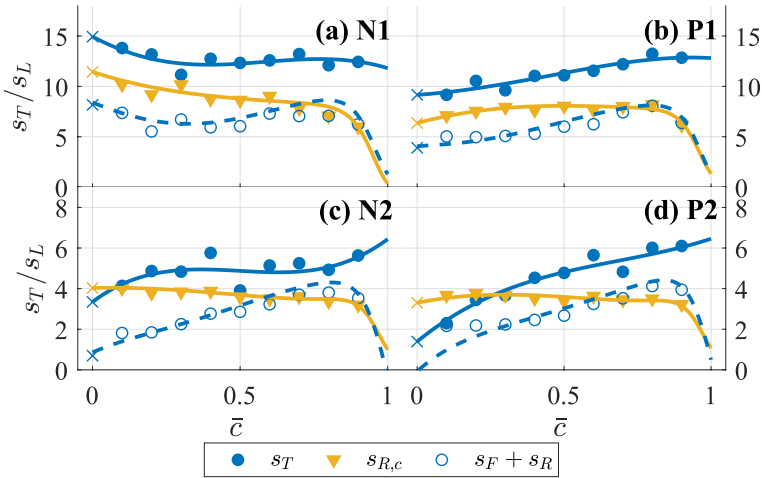


**Fig. 18** Closure of the balance of mean progress of reaction [Eq. (5)] including the correction factor  $\bar{\omega}_{c,f}/\bar{\omega}_c$  along streamlines in Case 1. Solid points: conditional average of measurement in Fig. 15. Solid line and dashed lines: fitted burning velocities derived from previous sections.  $s_T, s_F$  are the same values as in Fig. 15. The corrected  $s_{R,c}$  was calculated as  $s_R/(\bar{\omega}_{c,f}/\bar{\omega}_c)$

of  $s_{R,c} + s_F$  is still not negligible but the difference now appears to be constant across the flame brush. Further corrections can be possibly suggested, such as the factor  $4/\pi$  for correcting from 2D to 3D FSD (Veynante et al. 2010; Zheng et al. 2023).

### 5 Conclusions

In this study, we have conducted an experimental investigation using Mie scatter iso-surface locations of the progress of reaction and velocity distributions simultaneously to reconstruct the different terms of the balance of the progress of reaction, and interpret variables based on the flame brush theory.

All terms of the balance reaction for the Favre-averaged progress variable in were measured and fitted using physical models to the leading edge so that turbulent burning velocities from different terms could be estimated across the flame brush region. A perfect closure of the independently measured terms in the balance equation could not be obtained along the selected streamlines. Specifically, discrepancies were found between  $s_T$  and the sum of three terms in the RHS of Eq. (5). The reaction terms, which are of leading order, decrease along streamlines. At the leading edge of  $\bar{c} = 0$ , the sum of  $s_F + s_R$  assumes values that appear almost twice as large as the measured displacement velocity,  $s_T$ . The curve of  $s_T$  intersects with the curve of the sum of  $s_F + s_R$  at around  $\bar{c} = 0.6 \sim 0.8$ , where turbulent flux terms are close to zero.

A hypothesis for the discrepancy is suggested considering inherent spatial filtering of the reaction rate term via the detection of the leading edge, as suggested in DNS studies. These studies show that the distortion of the mean reaction rates can only be neglected for filter sizes significantly smaller than the flame thickness. In the present case, this

means that edge resolutions of at least a factor of 5 better than the current values is necessary to resolve the reaction rate terms adequately. Whereas this may be possible for the iso-curves of scalars (e.g. using Rayleigh or OH PLIF imaging), the simultaneous measurements of velocities cannot currently reach those levels of resolution.

## 6 Supplementary Information

A supplementary documents is attached, including details of deriving and measuring the molecular diffusion velocities  $s_D$ , the equivalence between the definition of FSD in Eq. (11) and FSD from area per volume.

### Appendix: Mass Conservation Along Streamlines

A measure of the fidelity of the measurements is that the mean mass flow rate indicated in should be constant along the identified streamtubes across the flame brush, starting at the leading edge,

$$d\dot{m} = \rho_u \bar{\mathbf{u}}_0 \cdot \mathbf{n} dA_0 = \bar{\rho} \bar{\mathbf{u}} \cdot \mathbf{n} dA_c = \rho_b \bar{\mathbf{u}}_1 \cdot \mathbf{n} dA_1 \tag{1}$$

$$\frac{d\dot{m}}{dA_0} = \bar{\rho} \bar{\mathbf{u}} \cdot \mathbf{n} \frac{dA_c}{dA_0} = \bar{\rho} |\bar{\mathbf{u}}| \cos(\alpha - \beta) \frac{dA_c}{dA_0} \tag{2}$$

The inner product  $\bar{\mathbf{u}} \cdot \mathbf{n}$  is converted into a product of  $|\bar{\mathbf{u}}|$  and the cosine of angle difference of the directing angles  $\alpha$  and  $\beta$ , which are obtained by a polynomial fits of Figs. 7 and 5. The area expansion ratio  $dA_c/dA_0$  is obtained from the 2D areas between streamlines, and the assumption of axisymmetric distribution.

For each streamline crossing an isocontour of  $\bar{c}$ , given by  $\bar{r}(\bar{z})$ , the expansion ratio  $dA_c/dA_0$  is given as:

$$dA_c = 2\pi \bar{r} d\bar{l} = 2\pi \bar{r} \frac{d\bar{z}}{\sin|\alpha|} \tag{3}$$

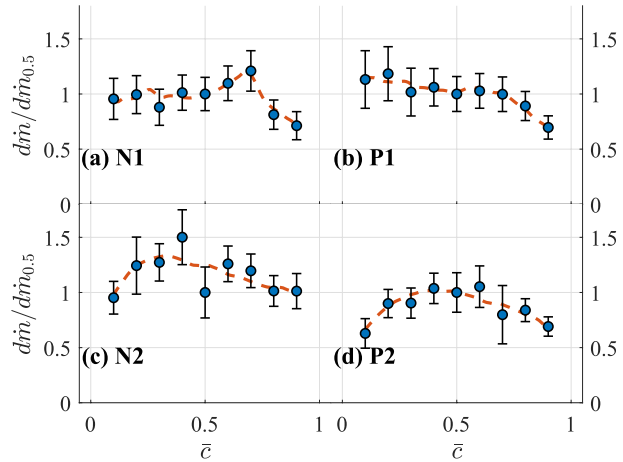
$$\frac{dA_c}{dA_0} = \frac{d\bar{z}_c \sin|\alpha|_0}{d\bar{z}_0 \sin|\alpha|_c} \tag{4}$$

where  $\alpha$  is the angle between the vertical  $z$ -axis and the local normal vector of the  $\bar{c}$ -isocontour defined in Fig. 5,  $d\bar{l}$  and  $d\bar{z}$  are the corresponding length and height for the chosen streamtube crossing. In the present work, the minimum spacing between streamlines at  $c = 0$  was taken as approximately 1 mm, as a compromise between convergence of the respective velocity value, and the smallest possible spatial resolution.

The corresponding uncertainty in  $dA_c$  is derived from invoking Eq. (13) into Eq. (4) by neglecting the correlation between  $r_0$  and  $dl = dz/\sin|\alpha|$ , and we have

$$\sigma_{\Delta A_c} \approx 2\pi \sqrt{(r_0 \sigma_{\Delta l})^2 + (\Delta l \sigma_{r_0})^2} \tag{5}$$

**Fig. 19** Mass flow rate along the streamline, normalized by the mass at  $\bar{c} = 0.5$ . Symbols are individual measurement points, and dashed red lines a polynomial fit. Error bars reflect uncertainties in measurements, dominated by the angle difference



$$= 2\pi \sqrt{\left(\frac{r_0 \Delta z}{\sin^2 |\alpha|} \sigma_{\sin |\alpha|}\right)^2 + \left(\frac{\Delta z}{\sin |\alpha|} \sigma_{r_0}\right)^2} \tag{6}$$

$$= 2\pi \sqrt{\left(\frac{r_0 \Delta z \cos \alpha}{\sin^2 |\alpha|} \sigma_\alpha\right)^2 + \left(\frac{\Delta z}{\sin |\alpha|} \sigma_{r_0}\right)^2} \tag{7}$$

The uncertainty of the cosine of the angle difference can be expressed as Eq. (8).

$$\sigma_{\cos(\alpha-\beta)} = \sigma_{(\alpha-\beta)} |\sin(\alpha-\beta)| = \sqrt{\sigma_\alpha^2 + \sigma_\beta^2 - 2\sigma_{\alpha\beta}} |\sin(\alpha-\beta)| \tag{8}$$

The uncertainty in the magnitude of  $\mathbf{u}$  was introduced in Sect. 3.5. Any correlation between velocity magnitudes, angles and area expansion assumed to be negligible, so the total uncertainty of the mass of  $\sigma_{dm/dA_0}$  in Eq. (2) can be written as Eq. (9). When normalized by the  $dm_{0.5}$  in Fig. 19, the uncertainty can be further written as Eq. 10

$$\sigma_{dm/dA_0} = \left| \frac{dm}{dA_0} \right| \sqrt{\left(\frac{\sigma_{\mathbf{u}}}{|\mathbf{u}|}\right)^2 + \left(\frac{\sigma_{dA_c}}{dA_c}\right)^2 + \left(\frac{\sigma_{\cos(\alpha-\beta)}}{\cos(\alpha-\beta)}\right)^2} \tag{9}$$

$$\sigma_{dm/dm_{0.5}} \approx \left| \frac{dm}{dm_{0.5}} \right| \sqrt{\left(\frac{\sigma_{dm/dA_0}}{dm/dA_0}\right)^2 + \left(\frac{\sigma_{dm_{0.5}/dA_0}}{dm_{0.5}/dA_0}\right)^2} \tag{10}$$

Figure 19 shows the ratio of mass flow rate in the streamtube per unit area along streamtubes according to Eq. (2), normalized by the mass flow rate per unit area at  $\bar{c} = 0.5$  where the measurements of the isocontours of  $\bar{c}$  have higher accuracy. One can observe that deviations of up to 30% are observed relatively to the mean value in the middle of the flame brush. Sources of fluctuation include errors in the identification of isocontour edges (Zheng et al. 2022), errors in mean velocity magnitude, and in particular, errors in velocity angle measurement along the streamtube.

**Supplementary Information** The online version contains supplementary material available at <https://doi.org/10.1007/s10494-024-00538-2>.

**Acknowledgements** The high frequency imaging equipment used in the experimental work was provided by EPSRC Grant No. EP/K035282/1. Lee Weller was supported by UKRI/EPSRC Grant EP/T030801/1. For the purpose of open access, the authors have applied a Creative Commons Attribution (CC-BY) licence to any Author Accepted Manuscript version arising from this submission.

**Author Contributions** YZ designed and performed the research, analyzed data and co-wrote the paper. LW aided with optical diagnostics in the execution of the experiments. SHb conceptualized and designed the research, and co-wrote the paper. The first draft of the manuscript was written by YZ and all authors commented on previous versions of the manuscript.

**Funding** This study was funded by EPSRC Grant No. EP/K035282/1 and UKRI/EPSRC Grant EP/T030801/1

**Availability of Data and Materials** All original data and processed data are available for sharing if published.

**Code Availability** All codes are available for sharing if published.

## Declarations

**Conflict of interest** The authors have no relevant financial or non-financial interests to disclose.

**Ethics Approval** The manuscript is only submitted on *Flow, turbulence and combustion* without being split into more than one part. No concurrent or secondary publication is conducted. Results are presented clearly, honestly, and without fabrication, falsification or inappropriate data manipulation (including image based manipulation). Authors adhere to discipline-specific rules for acquiring, selecting and processing data by their own. This study is not related to creation of harmful consequences of biological agents or toxins, disruption of immunity of vaccines, unusual hazards in the use of chemicals, weaponization of research/technology.

**Consent for Publication** The authors all agreed with the publication.

**Open Access** This article is licensed under a Creative Commons Attribution 4.0 International License, which permits use, sharing, adaptation, distribution and reproduction in any medium or format, as long as you give appropriate credit to the original author(s) and the source, provide a link to the Creative Commons licence, and indicate if changes were made. The images or other third party material in this article are included in the article's Creative Commons licence, unless indicated otherwise in a credit line to the material. If material is not included in the article's Creative Commons licence and your intended use is not permitted by statutory regulation or exceeds the permitted use, you will need to obtain permission directly from the copyright holder. To view a copy of this licence, visit <http://creativecommons.org/licenses/by/4.0/>.

## References

- Anderson, J.D., Wendt, J.: Computational Fluid Dynamics, vol. 206. Springer (1995)
- Bray, K.: Turbulent flows with premixed reactants. Turbulent reacting flows, pp. 115–183 (2005)
- Bray, K., Moss, J.B.: A unified statistical model of the premixed turbulent flame. *Acta Astronaut.* **4**(3–4), 291–319 (1977)
- Bray, K., Libby, P.A., Moss, J.: Flamelet crossing frequencies and mean reaction rates in premixed turbulent combustion. *Combust. Sci. Technol.* **41**(3–4), 143–172 (1984)
- Chakraborty, N., Alwazzan, D., Klein, M., et al.: On the validity of Damköhler's first hypothesis in turbulent Bunsen burner flames: a computational analysis. *Proc. Combust. Inst.* **37**(2), 2231–2239 (2019)
- Cheng, R., Shepherd, I.: The influence of burner geometry on premixed turbulent flame propagation. *Combust. Flame* **85**(1–2), 7–26 (1991)

- Dunstan, T.D., Swaminathan, N., Bray, K.N., et al.: Geometrical properties and turbulent flame speed measurements in stationary premixed V-flames using direct numerical simulation. *Flow Turbul. Combust.* **87**(2), 237–259 (2011)
- Dunstan, T., Swaminathan, N., Bray, K.: Influence of flame geometry on turbulent premixed flame propagation: a DNS investigation. *J. Fluid Mech.* **709**, 191–222 (2012)
- Filat'ev, S.A., Driscoll, J.F., Carter, C.D., et al.: Measured properties of turbulent premixed flames for model assessment, including burning velocities, stretch rates, and surface densities. *Combust. Flame* **141**(1–2), 1–21 (2005)
- Gambill, W.R.: How to estimate mixtures viscosities. *Chem. Eng.* **66**, 151–152 (1959)
- Goodwin, D.G., Speth, R.L., Moffat, H.K., et al.: Cantera: an object-oriented software toolkit for chemical kinetics, thermodynamics, and transport processes (2021). <https://www.cantera.org>. <https://doi.org/10.5281/zenodo.4527812>, version 2.5.1
- Gouldin, F.: Combustion intensity and burning rate integral of premixed flames. In: Symposium (International) on Combustion, pp. 381–388. Elsevier (1996)
- Kalt, P.A., Frank, J.H., Bilger, R.W.: Laser imaging of conditional velocities in premixed propane-air flames by simultaneous OH PLIF and PIV. In: Symposium (International) on Combustion, pp. 751–758. Elsevier (1998)
- Kalt, P.A., Bilger, R.W.: Experimental characterisation of the  $\alpha$ -parameter in turbulent scalar flux for premixed combustion. *Combust. Sci. Technol.* **153**(1), 213–221 (2000)
- Karpetis, A.N., Barlow, R.S.: Measurements of flame orientation and scalar dissipation in turbulent partially premixed methane flames. *Proc. Combust. Inst.* **30**(1), 665–672 (2005)
- Kheirkhah, S., Gülder, Ö.L.: Consumption speed and burning velocity in counter-gradient and gradient diffusion regimes of turbulent premixed combustion. *Combust. Flame* **162**(4), 1422–1439 (2015)
- Klein, M., Alwazzan, D., Chakraborty, N.: A direct numerical simulation analysis of pressure variation in turbulent premixed Bunsen burner flames-part 1: scalar gradient and strain rate statistics. *Comput. Fluids* **173**, 178–188 (2018)
- Klein, M., Kasten, C., Chakraborty, N., et al.: Turbulent scalar fluxes in H<sub>2</sub>-air premixed flames at low and high Karlovitz numbers. *Combust. Theor. Model.* **22**(6), 1033–1048 (2018)
- Kobayashi, H., Tamura, T., Maruta, K., et al.: Burning velocity of turbulent premixed flames in a high-pressure environment. In: Symposium (International) on Combustion, pp. 389–396. Elsevier (1996)
- Kobayashi, H., Seyama, K., Hagiwara, H., et al.: Burning velocity correlation of methane/air turbulent premixed flames at high pressure and high temperature. *Proc. Combust. Inst.* **30**(1), 827–834 (2005)
- Ku, H.H., et al.: Notes on the use of propagation of error formulas. *J. Res. Natl. Bur. Stand.* **70**(4), 263–273 (1966)
- Libby, P.A., Bray, K.: Countergradient diffusion in premixed turbulent flames. *AIAA J.* **19**(2), 205–213 (1981)
- Libby, P.A., Williams, F.A.: *Turbulent Reacting Flows*. Academic Press (1994)
- Lipatnikov, A., Chomiak, J.: Effects of premixed flames on turbulence and turbulent scalar transport. *Prog. Energy Combust. Sci.* **36**(1), 1–102 (2010)
- Louch, D., Bray, K.: Vorticity and scalar transport in premixed turbulent combustion. In: Symposium (International) on Combustion, pp. 801–810. Elsevier (1998)
- Miles, P.C.: Conditional velocity statistics and time-resolved flamelet statistics in premixed turbulent V-shaped flames. Ph.D. thesis, Cornell University (1991)
- Most, D., Dinkelacker, F., Leipertz, A.: Direct determination of the turbulent flux by simultaneous application of filtered Rayleigh scattering thermometry and particle image velocimetry. *Proc. Combust. Inst.* **29**(2), 2669–2677 (2002)
- Moureau, V., Domingo, P., Vervisch, L.: From large-eddy simulation to direct numerical simulation of a lean premixed swirl flame: Filtered laminar flame-pdf modeling. *Combust. Flame* **158**(7), 1340–1357 (2011)
- Mukhopadhyay, S., Bastiaans, R., van Oijen, J., et al.: Analysis of a filtered flamelet approach for coarse DNS of premixed turbulent combustion. *Fuel* **144**, 388–399 (2015)
- Peters, N.: *Turbulent Combustion*. Cambridge University Press (2000)
- Pfandler, S., Beyrau, F., Leipertz, A.: Flame front detection and characterization using conditioned particle image velocimetry (CPIV). *Opt. Express* **15**(23), 15444–15456 (2007)
- Poinsot, T., Veynante, D.: *Theoretical and Numerical Combustion*. RT Edwards Inc, Morningside (2005)
- Raffel, M., Willert, C.E., Scarano, F., et al.: *Particle Image Velocimetry: A Practical Guide*. Springer (2018)
- Rasool, R., Klein, M., Chakraborty, N.: Flame surface density based mean reaction rate closure for Reynolds averaged Navier–Stokes methodology in turbulent premixed Bunsen flames with non-unit Lewis number. *Combust. Flame* **239**, 111766 (2022)

- Sankaran, R., Hawkes, E.R., Chen, J.H., et al.: Structure of a spatially developing turbulent lean methane-air Bunsen flame. *Proc. Combust. Inst.* **31**(1), 1291–1298 (2007)
- Shepherd, I., Bourguignon, E., Michou, Y., et al.: The burning rate in turbulent Bunsen flames. In: *Symposium (International) on Combustion*, pp. 909–916. Elsevier (1998)
- Shepherd, I.: Flame surface density and burning rate in premixed turbulent flames. In: *Symposium (International) on Combustion*, pp. 373–379. Elsevier (1996)
- Shepherd, I., Cheng, R.K., Talbot, L.: Experimental criteria for the determination of fractal parameters of premixed turbulent flames. *Exp. Fluids* **13**(6), 386–392 (1992)
- Skiba, A.W., Carter, C.D., Hammack, S.D., et al.: Experimental assessment of the progress variable space structure of premixed flames subjected to extreme turbulence. *Proc. Combust. Inst.* **38**(2), 2893–2900 (2021)
- Smith, G.P., Golden, D.M., Frenklach, M., et al.: Gri 3.0 mechanism. Gas Research Institute. [http://www.me.berkeley.edu/gri\\_mech](http://www.me.berkeley.edu/gri_mech) (1999)
- Steinberg, A.M., Driscoll, J.F., Ceccio, S.L.: Measurements of turbulent premixed flame dynamics using cinema stereoscopic PIV. *Exp. Fluids* **44**(6), 985–999 (2008)
- Sweeney, M.S., Hochgreb, S., Dunn, M.J., et al.: Multiply conditioned analyses of stratification in highly swirling methane/air flames. *Combust. Flame* **160**(2), 322–334 (2013)
- Troiani, G., Battista, F., Picano, F.: Turbulent consumption speed via local dilatation rate measurements in a premixed Bunsen jet. *Combust. Flame* **160**(10), 2029–2037 (2013)
- Veynante, D., Piana, J., Duclos, J., et al.: Experimental analysis of flame surface density models for premixed turbulent combustion. In: *Symposium (International) on Combustion*, pp. 413–420. Elsevier (1996)
- Veynante, D., Lodato, G., Domingo, P., et al.: Estimation of three-dimensional flame surface densities from planar images in turbulent premixed combustion. *Exp. Fluids* **49**(1), 267–278 (2010)
- Vreman, A., Van Oijen, J., De Goey, L., et al.: Subgrid scale modeling in large-eddy simulation of turbulent combustion using premixed flamelet chemistry. *Flow Turbul. Combust.* **82**(4), 511–535 (2009)
- Wabel, T.M.: An Experimental Investigation of Premixed Combustion in Extreme Turbulence. Ph.D. thesis, University of Michigan (2017)
- Wieneke, B.: PIV uncertainty quantification from correlation statistics. *Meas. Sci. Technol.* **26**(7), 074002 (2015)
- Yuen, F.T.C.: Experimental investigation of the dynamics and structure of lean-premixed turbulent combustion. Ph.D. thesis, University of Toronto, Canada (2009)
- Zheng, Y., Weller, L., Hochgreb, S.: Instantaneous flame front identification by Mie scattering vs. OH PLIF in low turbulence Bunsen flame. *Exp. Fluids* **63**(5), 1–16 (2022)
- Zheng, Y., Weller, L., Hochgreb, S.: 3D Flame surface density measurements via orthogonal cross-planar MIE scattering in a low-turbulence Bunsen flame. *Proc. Combust. Inst.* **39**(2), 2369–2377 (2023)

**Publisher's Note** Springer Nature remains neutral with regard to jurisdictional claims in published maps and institutional affiliations.

## Authors and Affiliations

Yutao Zheng<sup>1</sup> · Lee Weller<sup>1</sup> · Simone Hochgreb<sup>1</sup>

✉ Yutao Zheng  
yz615@cam.ac.uk

Lee Weller  
lw493@cam.ac.uk

Simone Hochgreb  
sh372@cam.ac.uk

<sup>1</sup> Department of Engineering, University of Cambridge, Trumpington Street, Cambridge CB21PZ, UK